

Capillary pressure and relative permeability estimation for low salinity waterflooding processes using pore network models

Edgar G. Martínez-Mendoza^{a,*}, Martín A. Díaz-Viera^b, Manuel Coronado^b, Ana T. Mendoza-Rosas^c

^a Universidad Nacional Autónoma de México, Ciudad de México, México

^b Instituto Mexicano del Petróleo, Eje Central Lázaro Cárdenas 152, 07730, Ciudad de México, México

^c CONACYT-Centro de Ingeniería y Desarrollo Industrial, Av. Playa Pie de la Cuesta 702, 76125, Querétaro, México

ARTICLE INFO

Keywords:

Low salinity waterflooding
Pore network modeling
Pore scale modeling
Capillary pressure
Relative permeability

ABSTRACT

In this work, the effect of low salinity waterflooding (LSWF) on capillary pressure and relative permeability is studied at pore scale. For this purpose, a pore-scale model implemented on OpenPNM is developed to describe fluid flow, salinity transport and wettability change in a pore network. The effect is studied by considering high salinity waterflooding followed by low salinity waterflooding. The system wettability change is introduced as modifications of the local contact angle that are induced by the water salinity reduction. These modifications are evaluated by calculating the contact angle change in each pore and throat of the network, and then integrating it. From this analysis, a methodology has been developed to study the LSWF impact on capillary pressure and relative permeability. This methodology has been successfully applied to two pore network cases available in an open rock data base; one network correspond to a sandstone and the other to a carbonate sample. The methodology developed here can be seen as a tool to complement laboratory tests needed to determine the efficiency of LSWF processes.

1. Introduction

Low salinity waterflooding (LSWF) is an enhanced oil recovery (EOR) technique that mobilizes oil by reducing the salinity or modifying the composition of the injected water. The LSWF is considered as a simple and economical oil recovery technique due to the easy access to low salinity water sources, such as seawater (Al-Shalabi and Sepehrnoori, 2016; Nasralla et al., 2018). The LSWF potential was first recognized by Yildiz and Morrow (1996) and Tang and Morrow (1997), when they observed additional oil recovery in lab sandstone core floodings that has depended on injected water composition. Since then, LSWF has been successfully proven in laboratory flooding tests in sandstone and carbonate cores (Yildiz and Morrow, 1996; Tang and Morrow, 1997; Austad, 2013; Sheng, 2014; Sohal et al., 2016; Al-Shalabi and Sepehrnoori, 2016; Mahani et al., 2017), as well as in multiple sandstone reservoirs (Webb et al., 2004, 2005; Jerauld et al., 2008; Yousef et al., 2012; Aladasani et al., 2014). In many results, the oil recovery could be increased when injected water salinity was much lower than formation water salinity. Different mechanisms to explain the low salinity effect have been proposed (Austad, 2013; Sheng, 2014;

Mahani et al., 2017). However, there is not yet a consensus on dominant LSWF mechanisms, and answers to many physics and chemistry questions are still pending (Sheng, 2014; Al-Shalabi and Sepehrnoori, 2016; Etemadi et al., 2017).

To date, several authors have simulated the LSWF process in lab cores (Jerauld et al., 2008; Wu and Bai, 2009; Mahani et al., 2011; Omekeh et al., 2012; Dang et al., 2013; Al-Shalabi and Sepehrnoori, 2016; Coronado and Díaz-Viera, 2017; Sanaei et al., 2018) using a mechanistic approach that parametrically modifies the relative permeability and capillary pressure curves as a function of salinity (Sheng, 2014). In all of these models, diverse macroscopic properties for the involved oil recovery mechanism were assumed. For example, they consider spatially homogeneous rock-fluid properties, such as surface tension and contact angle, that importantly affect the capillary pressure and relative permeability curve behavior, which are key inputs in simulations. An alternative approach to evaluate the change on the capillary pressure and relative permeability due to LSWF is modeling the fluid flow and salinity transport at pore scale, which is the purpose of this work.

In general, pore-scale modeling is constituted by three main

* Corresponding author.

E-mail addresses: edgarg.martinezm@gmail.com (E.G. Martínez-Mendoza), mdiazv@imp.mx (M.A. Díaz-Viera), mcoronad@imp.mx (M. Coronado), ana.mendoza@cidesi.edu.mx (A.T. Mendoza-Rosas).

<https://doi.org/10.1016/j.petrol.2019.106253>

Received 9 April 2019; Received in revised form 5 July 2019; Accepted 7 July 2019

Available online 10 July 2019

0920-4105/ © 2019 Elsevier B.V. All rights reserved.

components: (i) description of the geometry and structure of the porous media, (ii) definition and solution of the governing equations, and (iii) selection of the macroscopic properties (Raouf, 2011). In this way, it is possible to incorporate porous medium properties that are underestimated at larger scales. Further, pore-scale modeling discretizes the porous structure by heterogeneously distributing voids with fluid phases inside, and its approaches are potentially attractive tools for dynamic property estimation, such as pore networks. Pore network modeling comprises various disciplines, such as spatial statistics, imaging and mathematical modeling, which contribute to characterize the desired phenomena, as is well described in examples given by M. Blunt and coworkers (Blunt et al., 2002, 2013; Okabe and Blunt, 2004; Valvatne et al., 2005; Gharbi and Blunt, 2012; Mostaghimi et al., 2012; Raeini et al., 2017, 2018; Xie et al., 2017). Part of Blunt's vast work focuses on imaging techniques and three-dimensional reconstructions applied in porous media. With these reconstructions and their coupling with mathematical models, Okabe and Blunt (2004); Valvatne et al. (2005); Mostaghimi et al. (2012) and Blunt et al. (2013) have studied Newtonian and non Newtonian flow in several rock samples (Okabe and Blunt, 2004; Valvatne et al., 2005; Mostaghimi et al., 2012; Blunt et al., 2013). In the same way, the pore network modeling application to other research areas includes: CO₂ sequestration (Kim and Santamarina, 2015), methane hydrate gas production (Mahabadi and Jang, 2014; Jang and Santamarina, 2014; Mahabadi et al., 2016), gas bubble nucleation/migration (Zhao and Ioannidis, 2011), water retention curves (Dai and Santamarina, 2013; Kang et al., 2016; Mahabadi et al., 2016), drying process in porous media (Yiotis et al., 2001), and polymer electrolyte membranes for fuel cells (Gostick et al., 2006, 2007; Gostick and Weber, 2015).

In the last two decades, EOR modeling via pore networks has grown importantly and acquired great interest. In principle, this is due to two main factors: the computational developments and the improvement in the detailed description rock-fluid systems. With a proper physical-mathematical formulation, the pore scale is able to capture some of the proposed EOR mechanisms that are not yet fully understood at larger scales, such as wettability alteration in rock-fluid systems. Bolandtaba and Skauge (2011) developed a network to study residual oil mobilization by polymer injection, where adsorption particle, entrapment by the polymer, and viscous forces were considered (Bolandtaba and Skauge, 2011). Hammond and Unsal (2012) and Qin and Hassanizadeh (2015) studied different mechanisms for microbial enhanced oil recovery, where the surfactants in the rock-fluid system produced oil mobilization and wettability change (Hammond and Unsal, 2012; Qin and Hassanizadeh, 2015). Lu and Yortsos (2001) established a model to simulate in situ combustion of forward filtration, where the porous microstructure and the solid fuel distribution effects on filtering combustion dynamics were investigated (Lu and Yortsos, 2001). Xu et al. (2018) modeled multiple physicochemical and thermal processes in combustion fronts in order to reduce potential risks in practical applications, such as high combustion temperature and low oxygen rate (Xu et al., 2018). Concerning the LSWF problem, Sorbie and Collins (2010) proposed a detailed semiquantitative theory, based on theoretical considerations at pore scale, of how the LSWF effect works (Sorbie and Collins, 2010). Subsequently, Watson et al. (2011) addressed an uncertainty assessment on wettability alteration, which is one of the most discussed LSWF mechanisms. The generated network allows one to carry out a systematic investigation of oil-water-rock parameters which are critical for oil recovery (Watson et al., 2011). Boujelben et al. (2018) described a dynamic model to investigate LSWF effects on oil recovery under dynamic flow conditions. Here, the salinity spatial distribution is tracked explicitly during the recovery process, and the fluid distribution is updated according to a relative balance between capillary and viscous forces. Further, the capillary effects are correlated to salinity by relating contact angle and local injected water concentration (Boujelben et al., 2018).

In this paper a systematic methodology to simulate the LSWF

process at pore scale is presented. This work is one of the first developments made to model LSWF using pore networks. The methodology will provide a tool to observe the salinity effects on effective flow properties, and using it the LSWF effect on capillary pressure and relative permeability curves is studied. This paper is structured as follows. First, the pore network modeling details are presented. Second, the proposed methodology for LSWF is discussed. Finally, two cases that show the methodology are presented. In these cases, fluid flow, salinity transport, and primary drainage are recreated to estimate absolute permeability, capillary pressure, and relative permeability curves.

2. Pore network modeling

Pore network modeling is an approach to study a wide range of phenomena, taking into account both the medium's geometry and its connectivity. One of the main applications is to estimate effective flow and transport properties, such as capillary pressure curves, effective permeabilities, and effective diffusion coefficient, among others, which regularly are obtained by laboratory tests and experimental correlations.

The pore network modeling discretizes the porous medium morphology which is composed by its internal structure and its topology (the way in which the medium is connected) (Sahimi, 2011). In principle, the internal structure, which represents porosity, is constituted by pores and throats. The pores are defined as the larger voids connected by narrower paths called throats (Blunt et al., 2013). In general, the key parts of a pore network model are the pore structure and the equations describing the phenomena, according to the study scale. The first part is commonly known as geometry, which expresses the medium connectivity and discretizes throats and pores by means of geometric entities (Aker et al., 1998). The second part is the mathematical modeling that describes the phenomena in porous media. Coupling these elements adequately will allow optimal estimates (Arns et al., 2004; Martínez-Mendoza, 2016). In this paper, these two main elements are decomposed in order to gain a better overall model understanding. The elements involved are: (i) network, (ii) geometry, (iii) phases, (iv) pore-scale physics, and (v) methods (see Fig. 1). The development of these five elements will enhance the overall pore network model. Briefly, each pore network element is described below.

2.1. Network

It is the set of spatially localized void sites connected by bonds (Raouf et al., 2013). The network is the element that denotes the medium connectivity, it supports the model geometry and serves as simulation mesh. An important network property is the coordination number. The coordination number z describes the connectivity between sites and bonds, which means the number of bonds connected to a site.

2.2. Geometry

Geometric entities placed in the network shape the internal medium structure. The network sites support the pores, while the bonds the throats. These elements can have both regular and irregular forms, being the former the one that offers a larger capability to describe the physical process. The irregular shapes can extend the study scope over processes that in a larger scale are negligible (Sahimi, 2011).

2.3. Phases

Depending on the process to be recreated, fluid or solid phases must be physically and chemically described by constitutive equations or correlations.

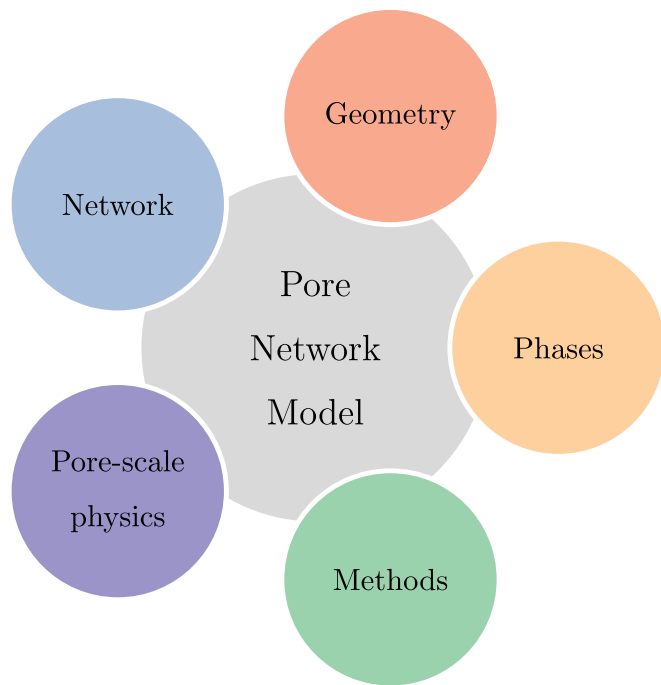


Fig. 1. In general, the key elements of a pore network model are the medium structure and the mathematical models, and their adequate coupling can describe the phenomena at pore scale. In this work, these main elements are decomposed into: (i) network, (ii) geometry, (iii) phases, (iv) pore-scale physics, and (v) methods.

2.4. Pore-scale physics and methods

To set the phase behavior at pore scale, the pore and throat geometry has to work together with proper definitions, physical laws, and constitutive equations; thus, suitable expressions for pore network models are obtained. All this is known as pore-scale physics (Ioannidis and Chatzis, 1993; Gostick et al., 2007). By employing these assumptions, it becomes easier to establish methods that describe the nature of the desired events. Here, the phenomena of interest are fluid flow, salinity transport, and immiscible displacement.

3. Fluid flow and salinity transport modeling in pore networks

The LSWF process will be modeled as a decoupled flow and transport problem. From the fluid flow problem, pore pressure values will be computed, and they will be used in the transport problem to estimate the salinity concentration in both pores and throats. The concentration values will shape the salinity state in the network. It should be mentioned that, by decoupling fluid flow from salinity transport we are neglecting some non-linear effects that salinity reduction could in turn affect the flow, such as brine viscosity alterations or pore/throat aperture modifications due to salinity changes.

3.1. Conceptual model

The mathematical model considers a porous medium discretized by pores that are connected by narrower paths called throats, whose pore and throat geometry is invariant in time. Further, it is assumed that, during the whole process the porous medium is completely occupied by a fluid phase which contains only one dissolved component. The fluid flow and salinity transport will be solved in a decoupled way. The fluid flow through the network is under saturated conditions assuming laminar, Newtonian and single-phase flow. After imposing a pressure gradient between two opposite boundaries, a flow field in the network

will take place. The salinity transport inside the system is considered to follow advective-diffusive processes. Each network element (pores and throats) will be taken as a control volume, and salinity mass balance is solved over each element. Finally, a fully mixed domain is considered both in pores and in throats, therefore, a constant salinity gradient is assumed.

3.2. Mathematical formulation

3.2.1. Fluid flow

The fluid flow through pore network models assumes the Hagen-Poiseuille law, which describes laminar flow, q , of an incompressible and Newtonian fluid, under a pressure drop effect:

$$q = -\frac{\pi r^4 \Delta p}{8\mu l} \quad (1)$$

where r is the conduit radius, l is the conduit length, μ is the fluid viscosity, and p is the pressure. From this expression, the fluid hydraulic conductance κ follows as:

$$\kappa = \frac{\pi r^4}{8\mu l} \quad (2)$$

Considering a mass balance over each pore in the network, and using Equation (1), yields:

$$\sum_{j=1}^n \kappa_{ij} (p_i - p_j) = 0 \quad (3)$$

where κ_{ij} is the total hydraulic conductance between pore i and pore j , whilst p_i and p_j are the pressures at each element. Equation (3) denotes the fluid flow model for pore networks. The total hydraulic conductance is computed as the hydraulic conductance sum through half of pore i , the connecting throat ij , and half of pore j . This parameter (κ_{ij}) depends on the size and the length of pores and throats.

Equation (3) sets up the system of algebraic equations for the pressure value at each pore of the network to be solved. By this way the equation set $A\mathbf{x} = \mathbf{b}$ is obtained, where A is a banded matrix constituted by the hydraulic conductivities κ_{ij} , \mathbf{x} is the pore pressure vector, and \mathbf{b} contains the boundary condition values. After solving the system, the pore network model permeability is obtained by Darcy's law:

$$K = \frac{\mu QL}{A(p_{in} - p_{out})} \quad (4)$$

where Q is the total flow across the network, A is the cross-sectional area normal to flow direction, L is the network length in the flow direction, p_{in} is the inlet pressure, and p_{out} is the outlet pressure.

3.2.2. Salinity transport

From the fluid flow problem, the pore pressure values are used to model the salinity advance via advective-diffusive transport.

For a given pore i , the one-component transport equation is:

$$V_i \frac{dc_i}{dt} + \sum_{j \in I_i} q_{ij} c_i - \sum_{j \in I_i} q_{ij} c_{ij} = \sum_{j \in I_i} D_e A_{ij} \frac{c_{ij} - c_i}{l_{ij}}, \quad \forall i \in [1, N_p] \quad (5)$$

where V_i and c_i are the volume and the salinity concentration for pore i , respectively. The flow rate and the salinity concentration throughout throat ij are denoted as q_{ij} and c_{ij} , respectively. D_e is the effective diffusion coefficient, A_{ij} is the connecting throat cross-sectional area, and l_{ij} is the connecting throat length. The total number of pores in the network is expressed as N_p , z_i is the pore coordination number, and I_i is the index set containing all the indexes of the pores connected to pore i through throat ij .

In the same way, the salinity transport equation for a given throat ij is:

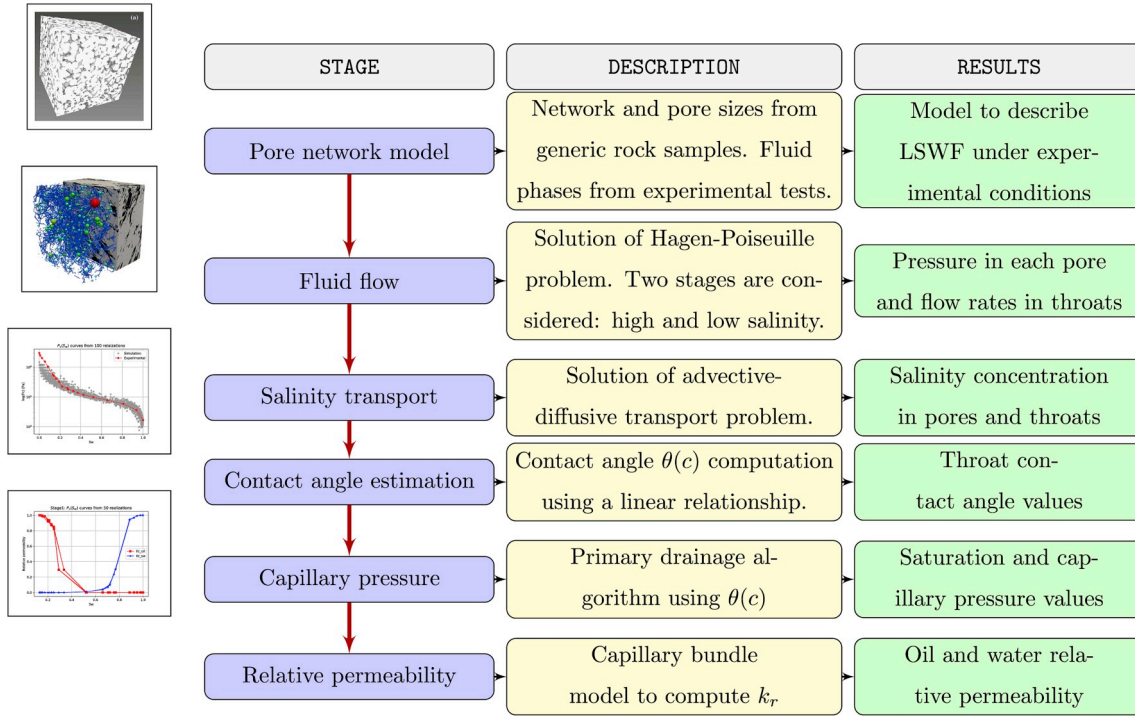


Fig. 2. Workflow using the pore network approach to investigate low salinity waterflooding.

$$V_{ij} \frac{dc_{ij}}{dt} + q_{ij}c_i + q_{ij}c_j - 2q_{ij}c_{ij} = D_e A_{ij} \frac{c_i - c_{ij}}{l_{ij}} + D_e A_{ij} \frac{c_j - c_{ij}}{l_{ij}},$$

$$\forall i \in [1, N] \quad (6)$$

where V_{ij} is the volume and c_{ij} is the salinity concentration applying to throat ij , respectively, and c_j is the salinity concentration within pore j .

Equation (5) and Equation (6) comprise the mathematical model of fluid flow and salinity transport for pore networks, and their corresponding initial and boundary conditions are given by:

$$c(I, t_0) = c_0$$

$$c(I_{inlet}, t \geq t_0) = c_{inlet}$$

$$\left. \frac{dc}{dx} \right|_{I_{outlet}, t \geq t_0} = 0 \quad (7)$$

where I is the set of pore and throat indexes. I_{inlet} and I_{outlet} are the indexes of pores placed at the inlet and the outlet boundaries, respectively. The initial salinity concentration is denoted as c_0 , while the salinity concentration at the inlet is c_{inlet} . The initial time is expressed as t_0 .

3.3. Numerical discretization

For discretization of the time derivative in the transport Equation (5) and Equation (6) a first order backward finite difference method is applied, resulting in a full implicit numerical scheme in time, which is unconditionally stable (Ewing and Wang, 2001). For a given pore i , the discretized Equation (5) can be written as:

$$V_i \frac{c_i^t - c_i^{t-1}}{\Delta t} = \sum_{j \in I_i} q_{ij} c_{ij}^t - \sum_{j \in I_i} q_{ij} c_i^t + \sum_{j \in I_i} D_e A_{ij} \frac{c_{ij}^t - c_i^t}{l_{ij}} \quad (8)$$

where the time step is denoted as Δt . Leaving only c_i^{t-1} on the left hand side of Equation (8), results:

$$c_i^{t-1} = c_i^t - \frac{\Delta t}{V_i} \left[\sum_{j \in I_i} q_{ij} c_{ij}^t - \sum_{j \in I_i} q_{ij} c_i^t + \sum_{j \in I_i} D_e A_{ij} \frac{c_{ij}^t - c_i^t}{l_{ij}} \right] \quad (9)$$

Similarly, the numerical discretization of Equation (6) for a given throat ij is:

$$c_{ij}^{t-1} = c_{ij}^t - \frac{\Delta t}{V_{ij}} \left[q_{ij} c_i^t + q_{ij} c_j^t - 2q_{ij} c_{ij}^t + D_e A_{ij} \frac{c_i^t - c_{ij}^t}{l_{ij}} + D_e A_{ij} \frac{c_j^t - c_{ij}^t}{l_{ij}} \right] \quad (10)$$

The discretized initial and boundary conditions applied to Equation (9) and Equation (10) are:

$$c_i = c_0, \quad \forall i \in I_{pore}, \quad t = t_0$$

$$c_{ij} = c_0, \quad \forall ij \in I_{throat}, \quad t = t_0$$

$$c_i = c_{inlet}, \quad \forall i \in I_{inlet}, \quad t \geq t_0$$

$$\sum_{j \in I_{outlet}}^{z_i} \frac{c_{ij}^t - c_i^t}{l_{ij}} = 0, \quad t \geq t_0 \quad (11)$$

where I_{pore} and I_{throat} are the indexes of pores and throats, respectively. Equation (9) and Equation (10) lead to a linear system $A\bar{x} = \bar{b}$, where the number of unknown variables is equal to the total number of pores and throats $N_p + N_t$. Additionally, for scheme stability, the minimum time step is chosen on the basis of throat residence times (Raof, 2011; Acharya et al., 2005):

$$\Delta t = \min \left\{ [V_{ij}] \left[q_{ij}^{-1} \right] \right\} = \min \{ T_{ij} \} \quad (12)$$

In Equation (12), T_{ij} expresses the fluid residence time within throat ij . Since the advective-diffusive transport processes drive the salinity fluxes, the smallest throat, with higher flux rate, sets the time step (Raof et al., 2014).

3.4. Computational implementation

The salinity transport model was implemented in OpenPNM which is an open-source pore network modeling package coded in Python. This package is fully independent of the network topology and dimensionality, since graph theory descriptors to represent the structure is used (Gostick et al., 2016). Furthermore, OpenPNM is designed to be customized; that is, users can code their own pore-scale physics and

Table 1

Information from an experimental test and Yousef et al. (2011) to set up Case 1 and Case 2, respectively.

Property	Case 1	Case 2	Unit
Core length, L	0.049	0.041	m
Core diameter, d	0.038	0.038	m
Porosity, ϕ	0.18	0.25	m^3/m^3
Absolute permeability, k	6.46E-14	3.91E-14	m^2
Temperature, T	363.15	373.15	K
Pressure, p	17.2	12.4	MPa
Cross-sectional area, A	1.14E-03	1.14E-03	m^2
Volume, V	5.71E-05	4.63E-05	m^3
Pore volume, PV	1.05E-05	1.16E-05	m^3

thermophysical property models (Fazeli et al., 2016; Sadeghi et al., 2017; Tranter et al., 2016, 2018). The validation of our implementation has been made against an 1D convective-dispersive solute transport equation provided by van Genuchten and Alves (1982) as described in Appendix A.

4. Workflow to study a LSWF process

In this work the LSWF modeling involves evaluating the salinity impact on capillary pressure and relative permeability. By following a pore network based methodology, which is described in Appendix B, a pore-scale physics to recreate a LSWF process is established (Martínez-Mendoza, 2018; Martínez-Mendoza and Díaz-Viera, 2018). The workflow to study LSWF processes is shown in Fig. 2 and listed as follows:

1. Pore network model: the network is mainly generated from imaging techniques. The open access data from two generic samples is used to set two case studies. The selection was based on the absolute permeability and the porosity values of the generic samples are close to information from experimental tests of our interest. The experiments study the injection of water with different salinity composition and its impact on oil recovery. Since these experiments were performed at lab scale, we only use their petrophysical information and description of the fluids to set our pore-scale models.
2. Fluid flow: to describe flow in the network, the model in Equation (3) is used, and the simulation parameters and conditions were taken from the experimental tests. After solving this equation, the pressure in each pore and the flow rate in throats are obtained.
3. Salinity transport: by using the previous pressure values, the salinity transport equations (Equation (5) and Equation (6)) are solved. As a result, the salinity concentration, at different simulation times, at each pore and throat in the network is obtained. This information

Table 2

Description of the pore network models used in case studies.

	Case 1	Case 2
	Sandstone Sample S1	Carbonate Sample C2-Yousef
Network	Irregular 1717 pores 2824 throats Volume = 1.76E-08 [m^3] Porosity = 14.35 (%) Absolute permeability = 1.53E-12 [m^2]	Irregular 4311 pores 7688 throats Volume = 9.77E-09 [m^3] Porosity = 24.41 (%) Absolute permeability = 3.76E-14 [m^2]
Geometry	Pores: spheres Throats: cylinders Cross section: circular Pore/throat sizes from imaging	Pore/throat sizes from distributions
Physics	Capillary pressure: Young-Laplace Hydraulic conductivity for cylinders	

will allow the evaluation of the injection of water with different salinity composition. It should be noted that, since salinity transport effect on fluid flow is negligible, the pressure field should be computed only once, at the workflow start.

4. Contact angle evaluation: the wettability is evaluated by considering a linear relationship between contact angle (θ) and salinity concentration (c). This evaluation is an attempt to assess the salinity impact on contact angle.
5. Capillary pressure: a primary drainage process is simulated, at each time step of the salinity transport problem, in which an interest oil is the invading fluid and the injected water is the defending phase. After determining the invasion sequence, i.e. the water-invaded pores and throats, the capillary pressure curves for oil and water systems are estimated. The primary drainage algorithm is based on invasion percolation theory to describe the fluid advance through the porous media, relating this event to properties of the system, and thus, recreating immiscible displacement processes (Broadbent and Hammersley, 1957; Dias and Wilkinson, 1986; Berkowitz and Ewing, 1998; Hunt and Ewing, 2009).
6. Relative permeability: the relative permeability curves are computed from the primary drainage invasion sequence and considering a capillary bundle model.

4.1. Salinity effect on contact angle

Wettability is the preferred tendency of a fluid to spread or adhere to a solid surface, in the presence of another immiscible fluid. A parameter that reflects such a preference is the contact angle θ . In pore-scale modeling, several mechanisms for wettability behavior have been proposed. In this work, the wettability change, and therefore the contact angle, is assumed as the principal consequence of LSWF effects. In principle, the throat initial contact angle value could be changed when low salinity water invades the throat. As a result, reduction in capillary forces, that could affect oil recovery, would be expected if the contact angle change modifies the wettability to a less oil-wet system (Boujelben et al., 2018). The following linear relationship between contact angle and salinity concentration is assumed (Aladasani et al., 2014):

$$\theta(c) = \theta^{HS} - \frac{c - c^{HS}}{c^{HS} - c^{LS}} (\theta^{HS} - \theta^{LS}) \quad (13)$$

where, θ^{HS} is the contact angle at the high salinity concentration, c^{HS} , and θ^{LS} is the contact angle at the low salinity concentration, c^{LS} .

4.2. Relative permeability

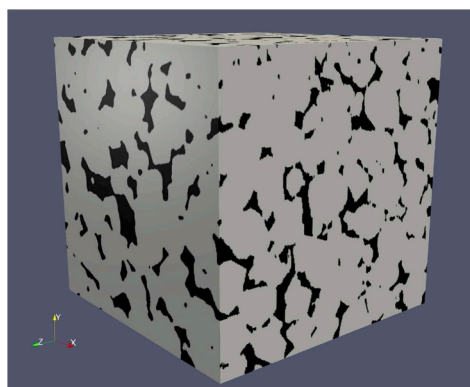
From the primary drainage capillary pressure and saturation data, we estimate the relative permeability curves using a bundle model. We consider the Rodríguez and Teyssier (1974) model which reproduces the displacement of a wetting fluid by a non-wetting fluid in porous media. The model can be written as:

$$j = \frac{\log\left(\int_{s_{wi}}^{s_w} \frac{ds_w}{p_c^2} / \int_{s_{wi}}^1 \frac{ds_w}{p_c^2}\right)}{\log\left(\frac{s_w - s_{wi}}{1 - s_{wi}}\right)} \quad (14)$$

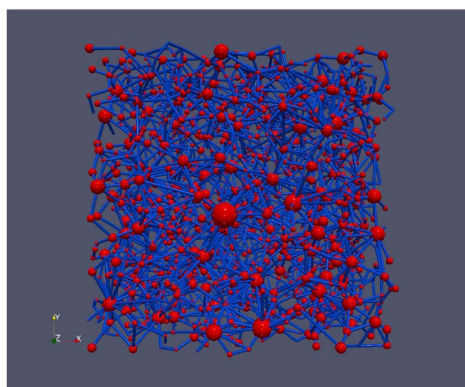
$$k_{rw} = \left(\frac{s_w - s_{wi}}{1 - s_{wi}}\right)^{2+j} \quad (15)$$

$$k_{rww} = \left[1 - \frac{s_w - s_{wi}}{1 - s_{wi}}\right]^2 \left[1 - \left(\frac{s_w - s_{wi}}{1 - s_{wi} - s_{rwi}}\right)^j\right] \quad (16)$$

where p_c is the capillary pressure, s_w is the wetting phase saturation, and s_{wi} is the irreducible wetting phase saturation. The subscript nw stands for the non-wetting phase. Finally, k_{rw} and k_{rww} refer to the wetting and the non-wetting phase relative permeability, respectively.



(a) Sandstone Sample S1 image



(b) Sandstone Sample S1 pore network model

Fig. 3. The generic sandstone Sample S1 used to simulate LSWF process in Case 1. (a) Micro CT image (ICL, 2014b). (b) Pore network model discretizing the sample, where spherical pores (red) and cylindrical throats (blue) are displayed. (For interpretation of the references to colour in this figure legend, the reader is referred to the Web version of this article.)

Table 3
Fluid properties used in Case 1.

Property	Oil	Formation water	Formation water	Unit	Reference
			diluted 100 times		
Density	881.6	1130.0	1013.8	kg/m ³	Experiment
Viscosity	1.08E-02	3.0E-04	4.85E-04	Pa. s	Experiment
Interfacial tension	–	0.0234	0.0172	N/m	Experiment
Contact angle	–	72	65	(°)	Moustafa et al. (2015)
Salinity concentration	–	216,000	2160	ppm	Experiment

Table 4
Parameters considered for LSWF process simulations.

Parameter	Case 1		Case 2		Unit
	HS	LS	HS	LS	
Injection time (t_{inj})			7000		s
Time step (Δt)			1		s
Initial salinity concentration (c_0)	0	c_{final}^{HS}	0	c_{final}^{HS}	ppm
Salinity concentration at inlet (c_{in})	216,000	2160	213,000	57,600	ppm
Neumann condition at outlet			0		ppm/m
Diffusion coefficient			2.15E-09		m ² /s

This model computes the relative permeability curves considering a characterization exponent obtained from capillary pressure data and the effective saturation data. The effective saturation of the non-wetting fluid is expressed as a relationship between the wetting fluid saturation and the space available for the non-wetting fluid (Rodríguez and Teyssier, 1974). Equation (14) is a Burdine-typed model which represents the pore space as a capillary bundle (Burdine, 1953; Li and Horne, 2006). In consequence, it meets the conditions of primary drainage algorithm and is suitable for the pore network approach.

5. Application to case studies

In this section the methodology is applied to two LSWF cases, one for sandstones and the other for carbonates. In the first case the capillary and relative permeability curves are calculated and fitted for a sandstone-oil-water system. LSWF test information and fluid properties were taken from an experimental test, while the rock sample characteristics were taken from literature. In the carbonate second case, data from a LSWF lab test and open access information were used. The objective of these applications are: 1) demonstrate the model capacity to simulate a LSWF process at pore scale, and 2) observe the salinity

effect on capillary pressure and relative permeability curves. The applications are described below. Finally, it should be emphasized that our flooding simulation procedure considers an initial condition in which the core is fully saturated with pure water. Then, the HS brine is injected, and after a steady-state is reached, the LS brine is introduced. This procedure has been employed to establish the starting distribution of high salinity water in the pore network, before the low salinity injection. This condition is different from considering a constant distribution of salt as initial condition, and in our case it can provide a better representation of the HS to LS transition.

5.1. Case 1: LSWF in a sandstone sample

This case seeks to introduce our methodology and shows a pore-scale LSWF study in sandstones. We use a laboratory test in a sandstone core, where additional oil recovery is observed after a sequential injection of formation water and 100-times diluted formation water. Further, open access information of a sandstone sample from a Middle East reservoir is used to generate the pore network model (Dong et al., 2007). However, not having the corresponding effective property measurements during the LSWF test (capillary pressure and relative permeability), our results establish an exploratory analysis on the expected values. The experimental test properties for Case 1 are summarized in Table 1.

In addition to the experimental test, we use the open access information of a generic sandstone sample from an Arabian reservoir (ICL, 2014b), which is here called Sample S1. Dong (2007) performed micro-computed tomography scanning of sandstone Sample S1 and several other rock samples (Dong, 2007). In this section, we use the extracted network and the pore and throat sizes from sandstone Sample S1, since its porosity and permeability values are close to those found in the sample of the experimental test. Details about the network model are presented in Table 2.

A network of 1717 pores and 2824 throats discretizes the sandstone Sample S1, and it is used in the next computations. Pores are assumed

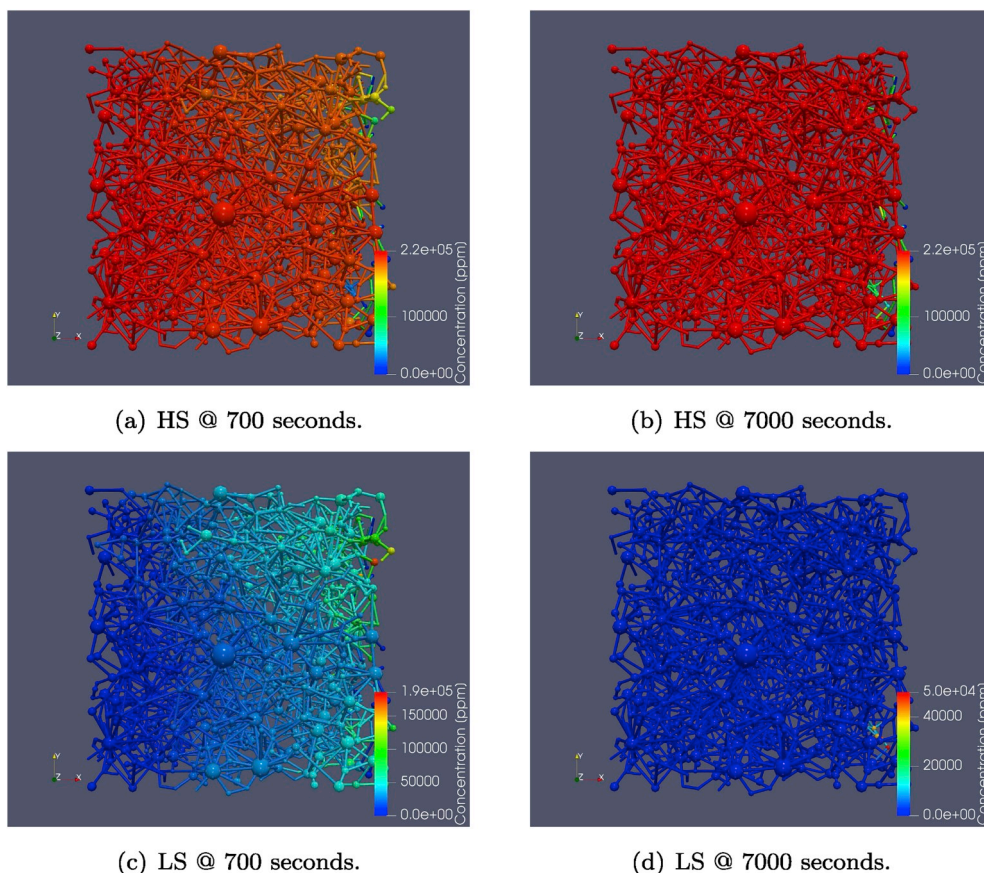


Fig. 4. Salinity concentration in sandstone Sample S1 network during LSWF simulation for Case 1. HS stage simulation at (a) 700 and (c) 7000 [s]. LS stage simulation at (b) 700 and (d) 7000 [s]. The water flows from left to right.

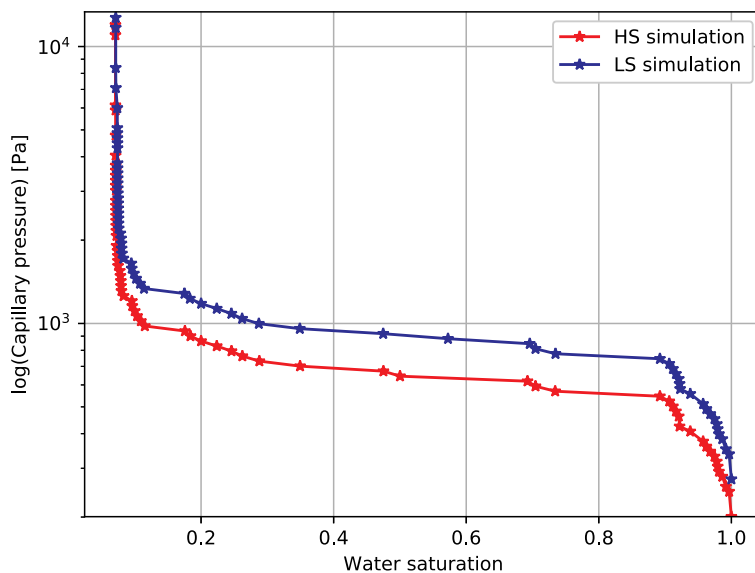
to be spheres, while throats are represented as cylinders. Both entities share a circular cross-section. The model porosity and permeability values are 14.35% and $1.53\text{E-}12 [m^2]$, respectively. The pore network model is shown in Fig. 3. Here, information from an experimental test was taken to establish the LSWF realization.

The LSWF simulation considers two brines that are injected sequentially into the network, which are formation water and formation water diluted 100 times. The formation water invades the network first, and corresponds to the high salinity concentration (HS). The low salinity fluid (LS) is the formation water diluted 100 times. The contact angle limiting values for high and low salinity were taken from Moustafa et al. (2015). Moustafa et al. (2015) investigated the effect of several nanomaterials on contact angle for a sandstone sample (Moustafa et al., 2015). Table 3 summarizes the fluid properties used in Case 1.

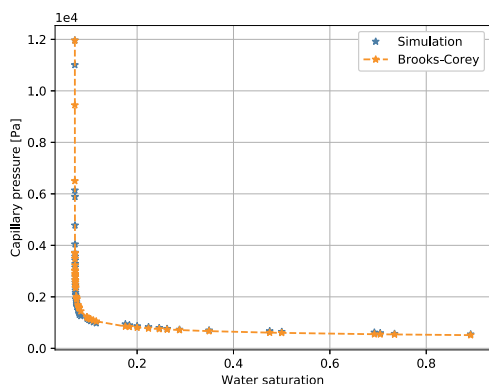
In the simulation, we solved the fluid flow and salinity transport problem in an uncoupled way; first the fluid flow is simulated in the network, and with the resulting pressure field the salinity transport is then computed. As explained before, the LSWF process begins invading the network (initially saturated with pure water) with formation water, during a given injection time t_{inj} . Later, the diluted water is injected to start the recovery stage. Therefore, at the simulation ending, different concentration states for each time step are obtained; salinity concentration values are known in each pore and throat. Our simulation considers a 4-h LSWF process, 7000 [s] each stage; additional information regarding the simulation is shown in Table 4. In general, during the first stage the salinity concentration in the network increases until a steady-state at high salinity is reached. By starting the low

salinity stage, the network concentration decreases, and most of the network elements reach the LS condition. Fig. 4 displays the salinity in the network during the HS and LS stages, at two simulation times. The salinity concentration values are used to calculate the throat contact angle, where Equation (13) is used, it shows that as salinity decreases, contact angle also does. The contact angle change modifies the network wettability to a less oil-wet system. At the LSWF process end, the network has a homogeneous contact angle distribution. In addition, there are no abrupt θ changes in throats. In the HS stage a value equal to 72° is reached, while in LS stage the value is 65° . Considering the contact angle as an amount that denotes the wettability degree, we find that the sandstone's wettability, in HS and LS, is homogeneous. The latter can favor the residual oil displacement and, thereby, increase the oil recovery factor.

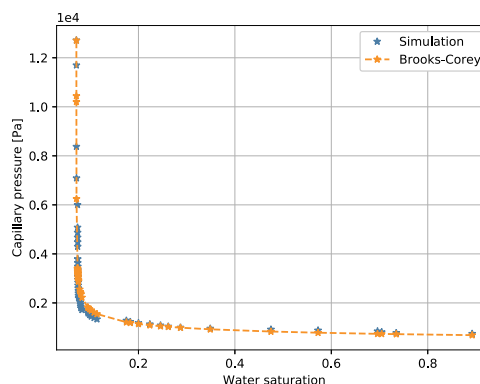
According to the limiting contact angle values for the high and low salinity states (72° and 65° , respectively), the system is slightly intermediate wet when the HS fluid is the invading phase. After we switch to the LS fluid, a wettability change in the network is observed. At the LSWF process end, the system has gained stronger affinity to water. The corresponding capillary pressure curves are shown in Fig. 5. The red curve in Fig. 5(a) gives the LS initial condition, where the capillary pressure values range from 0.2 to 12 [kPa]. When the LS stage finishes (curve in blue), the irreducible water saturation is almost the same as the initial condition, with a value equal to 7%. However, higher pressure values are required to displace oil when the LSWF ends. It follows that the LSWF gives place to a slightly wettability modification in the network, because the LSWF produces an increase in preference towards water. Subsequently, we fitted a Brooks-Corey model to the initial and



(a) Capillary pressure



(b) Fitted HS capillary pressure curve



(c) Fitted LS capillary pressure curve

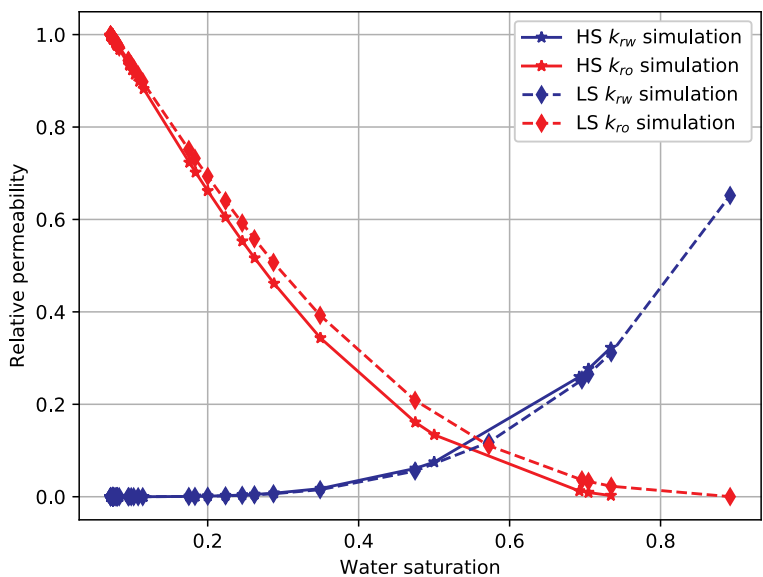
Fig. 5. Capillary pressure curves for Case 1. (a) Capillary pressure curves showing the LSWF effect. The red curve is for the HS, while the blue curve for LS. In (b) and (c) the fitted Brooks-Corey $p_c(s_w)$ models for HS and LS, respectively. The blue points represent the values calculated in the primary drainage algorithm. The orange points are obtained using the fitted model. The dashed orange line shows the fitted curve trend. (For interpretation of the references to colour in this figure legend, the reader is referred to the Web version of this article.)

Table 5
Fitting parameters for capillary pressure and relative permeability in HS and LS.

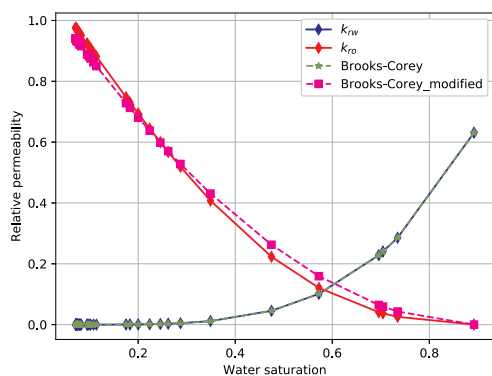
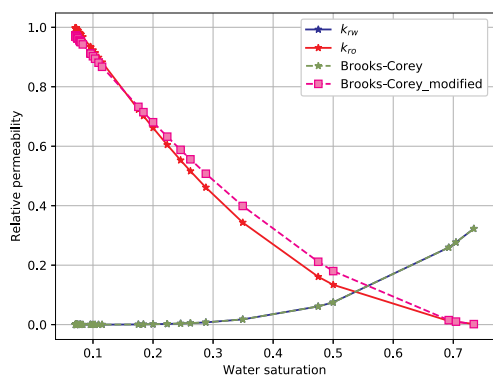
Parameter	Case 1		Case 2	
	HS	LS	HS	LS
Capillary pressure exponent	4.05	3.62	1.78	1.24
Entry pressure [Pa]	536	683	989	1002
Water endpoint (k_{rw}^0)	0.35	0.65	0.15	0.40
Oil endpoint (k_{ro}^0)	0.97	0.96	0.98	0.99
Water exponent (n_w)	3.36	3.77	4.00	3.87
Oil exponent (n_o)	1.69	1.91	1.45	2.00
Residual water saturation (s_{wr})	0.07	0.07	0.26	0.27
Residual oil saturation (s_{or})	0.25	0.1	0.25	0.1

final LS curves. The fitted models can be used in simulations at larger scales. Table 5 summarizes the fitted Brooks-Corey parameters, and plots Fig. 5(b) and (c) show the fitted curves and the original data points.

Fig. 6(a) shows the estimated relative permeability curve, the solid lines are for HS and the dashed for LS. In the HS period, a residual oil saturation equal to 0.25 is obtained. The k_r curve crossing takes place when the water saturation s_w^{cross} is 0.53, in which $k_{ro}^{cross} = k_{rw}^{cross} = 0.11$. Further, the water and oil relative permeability endpoint is 0.32 and 0.97, respectively. For $s_w < 0.4$, k_{rw} values are almost zero, this points to a mixed wet system. In the LS stage, these properties undergo minimal changes. The s_{or} value decreases 60 percent, $s_{or} = 0.1$. The k_r curve crossing point occurs at a $s_w^{cross} = 0.57$, with $k_r = 0.11$. The curve endpoints are 0.96 and 0.65 for oil and water, respectively. This behavior is consistent with the wettability change in capillary pressure.

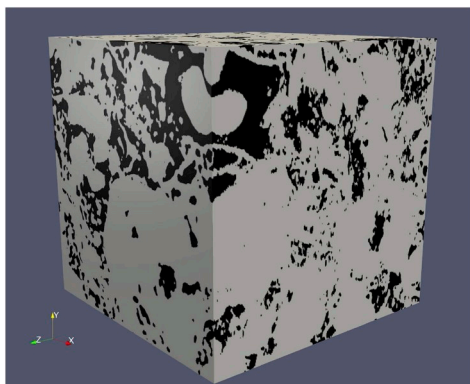


(a) Relative permeability

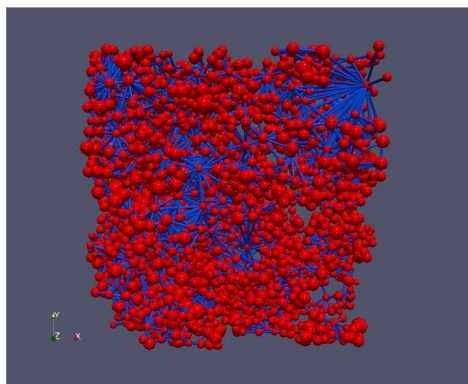


(b) Fitted HS relative permeability curve (c) Fitted LS relative permeability curve

Fig. 6. Relative permeability curves for Case 1. (a) The red lines show the oil relative permeability k_{ro} and the blue lines the water relative permeability k_{rw} . Solid lines correspond to HS and dashed lines to LS, and original data are in red and blue. The curves were fitted at the end of the (b) HS and (c) LS stages. In curve fitting, a Brooks-Corey k_{rw} model (green line) and a modified Brooks-Corey k_{ro} model (pink line) were used. (For interpretation of the references to colour in this figure legend, the reader is referred to the Web version of this article.)



(a) Carbonate C2 image



(b) C2-Yousef pore network model

Fig. 7. The synthetic carbonate Sample C2-Yousef used to simulate LSWF process in Case 2. (a) Micro CT image showing the carbonate C2 pore structure. (b) Pore network model C2-Yousef based on C2 structure. Spherical pores (red) and cylindrical throats (blue) are employed. (For interpretation of the references to colour in this figure legend, the reader is referred to the Web version of this article.)

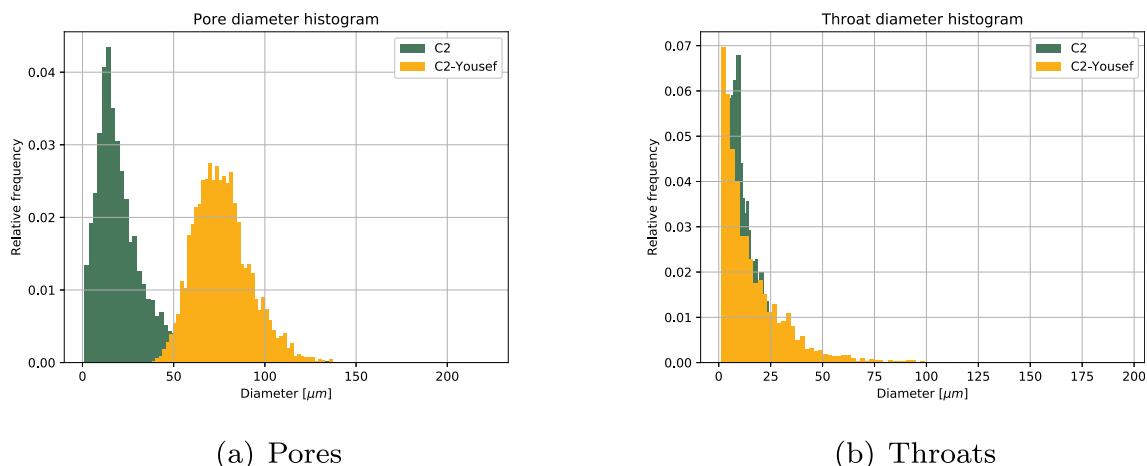


Fig. 8. Pore and throat diameter histograms. (a) Comparison between C2 (green) and C2-Yousef (orange) pore diameters, and (b) the corresponding histograms for throat diameters. (For interpretation of the references to colour in this figure legend, the reader is referred to the Web version of this article.)

Table 6
Probability distributions for pore and throat diameters in Case 2.

Property	Distribution	Shape	Location	Scale
C2 pores	Lognormal	0.6	-1.5	11
C2-Yousef pores	Lognormal	0.2	0	75
C2 throats	Lognormal	0.7	-0.3	5
C2-Yousef throats	Lognormal	0.9	1	30

Table 7
Fluid properties used in Case 2.

Property	Oil	Formation water	Seawater	Units	Reference
Density	873.0	1108.3	1015.2	kg/m^3	Yousef et al. (2011)
Viscosity	1E-03	4.76E-04	2.72E-04	$Pa \cdot s$	
Interfacial tension	-	0.0397	0.0339	N/m	
Contact angle	-	92	80	($^\circ$)	
Salinity concentration	-	213,000	57,600	ppm	

Finally, from the stage end, we fitted a Brooks-Corey k_{rw} model and a modified Brooks-Corey k_{ro} model to the estimated curves. The fitted curves are shown in Fig. 6(b) and (c), and their respective parameters are summarized in Table 5.

5.2. Case 2: LSWF in a carbonate sample

In this case we evaluate the LSWF impact on capillary pressure and relative permeability curves of a carbonate rock sample. Here we employ laboratory data from Yousef et al. (2011) and take the data for connate water and seawater for HS and LS, respectively, as well the data for viscosity, interfacial tension, contact angle, and salinity concentration. We use open access information from a generic carbonate sample described as C2 (see Fig. 7(a)) (ICL, 2014a), and we fitted probability distribution functions for C2 pore and throat sizes. Subsequently, the fitted distribution parameters were modified, in order to reproduce the porosity and permeability values of Yousef et al. (2011). We straightforwardly use the C2 extracted network without any modification, keeping the network topology invariant, thus the proper carbonate topology is ensured. By using the extracted network in combination with the fitted probability distribution, a new carbonate sample version is obtained, which is labeled as C2-Yousef in Fig. 7(b).

Fig. 8 shows the probability distribution functions for pore and throat size comparison between the carbonate C2 and the synthetic sample C2-Yousef. Fig. 8(a) presents the pore diameter histograms, and Fig. 8(b) shows the corresponding histograms for throat diameters. The carbonate C2 pore/throat diameters are those obtained and reported by Dong (2007). On the other hand, the diameter values for the C2-Yousef network were generated by probability distributions. The pore and throat size distribution of sample C2-Yousef was established by fitting a distribution to the original carbonate C2 data and then disturbing the fitting parameters. The distribution parameter selection was made in a deterministic way until reaching absolute permeability and porosity values similar to Yousef et al. (2011). It is important to note that no spatial dependence is considered in this process. Table 6 summarizes the probability distribution parameters for samples C2 and C2-Yousef.

The C2-Yousef network model consists of 8508 pores and 9818 throats, which are represented by spheres and cylinders, respectively. The model description is summarized in Table 2. In general, the network has highly dense areas of pores and throats, as well as considerable empty regions. This is attributed to the underlying complexity of carbonate pore structures. For this issue, image processing techniques have to treat microporosity and fractures in carbonates. In addition, if we wish to represent the porous structure by means of more complex pores and throats, it is necessary to take into account other geometric properties, such as angularity, inscribed and effective diameter, and shape factor. This new information can only be obtained from high-resolution imaging techniques.

The simulation considers formation water with HS concentration (213,000 [ppm]), while seawater is the LS fluid, whose concentration is almost a quarter of that of HS (57,600 [ppm]). In addition, we use the same injection time and time step values from Case 1 (see Table 4). The injected water information, for HS and LS, was taken from Yousef et al. (2011), whose fluid property values are displayed in Table 7.

Fig. 9 shows the salinity concentration in the network C2-Yousef during LSWF simulation. It is observed that, the water injection through the network is from left to right. According to the chosen time step, when the high salinity waterflooding (HSWF) ends, inlet pores and some neighboring pores reach the HS concentration (213,000 [ppm]), and a progressive concentration change in the network is observed. On the other hand, at the end of the LS process, most of the network has a concentration close to 60,000 [ppm]. It is noteworthy the existence of pores and throats with concentration values being almost zero in both recovery processes (HS and LS). Intuitively, this is attributed to small

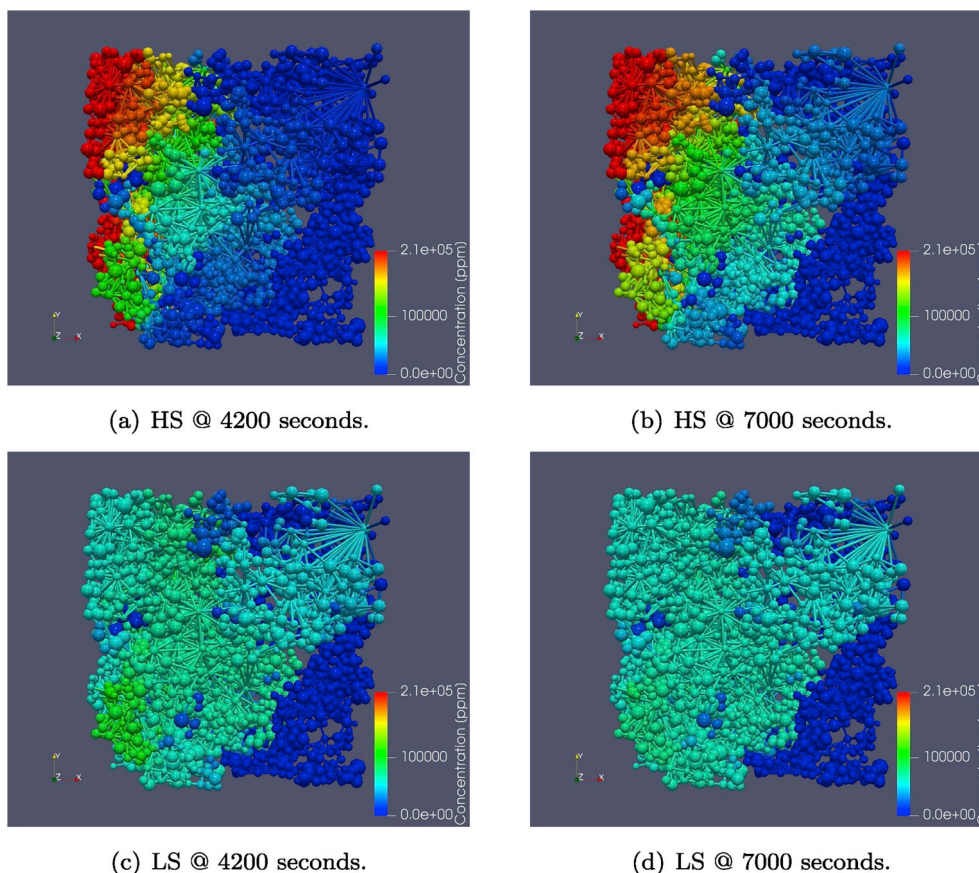


Fig. 9. Salinity concentration in C2-Yousef network during LSWF simulation for Case 2. HS stage simulation at (a) 4200 and (c) 7000 [s]. LS stage simulation at (b) 4200 and (d) 7000 [s]. The water flows from left to right.

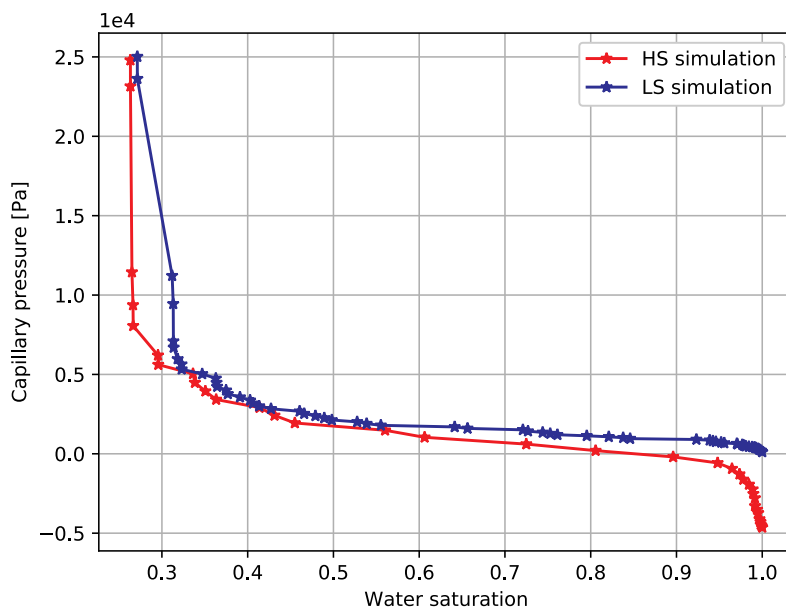
enough throat sizes to constrain advective transport effects. In principle, for this particular case, these pores and throats constitute no-flow zones which do not contribute for computing the absolute permeability.

By running primary drainage algorithm uncoupled from the salinity transport, capillary pressure curves for each time step are estimated, and they are shown in Fig. 10. In this way, it is observe how the network salinity, which represents the LSWF process, displaces and modifies the capillary pressure curves. We link this event to a wettability change. At this scale, the wettability change impacts on modifying or reestablishing preferential flow zones, as well as an oil redistribution, since the capillary pressure in a given throat can be increased or decreased (Boujelben et al., 2018).

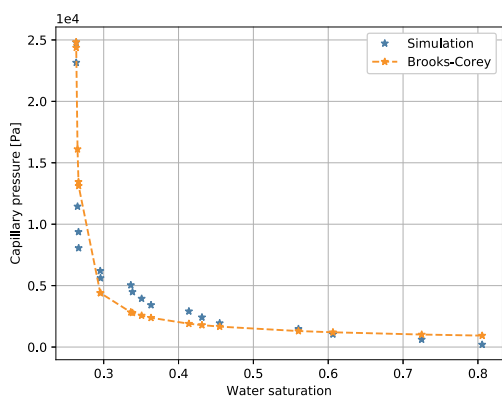
At the HS stage end, the C2-Yousef system remains with an intermediate wettability, but slightly preferring an oil contact; the maximum throat contact angle value is $92^\circ > 90^\circ$. Fig. 10(a) shows this effect, where the red curve is for the HSWF end, and in turn is the LSWF start. In this curve, capillary pressure values range from -5 to 25 [kPa]. This negative to positive value transition points out that oil prefers to be attached to the rock surface, when the system is totally saturated by water ($s_w \rightarrow 1$). As water saturation decreases, pressure increases and becomes positive. Therefore, the capillary pressure is positive and the wettability system changes from slightly oil wet to less oil wet, when $s_w < 0.8$. Subsequently, when the LS stage is completed, the capillary pressure curve is positive and shows an even less oil wettability (curve in blue). In general, at the LSWF end, the system has a slight preference towards water; that is, a minor wettability alteration occurs due to the

LSWF process. However, it is difficult to establish a clear and significant wettability change for this case study, given that the contact angle value range ($92^\circ - 76^\circ$) is for intermediate wettability. Fig. 10(b) and (c) show the fitted $p_c(s_w)$ models for HS and LS, respectively, and Table 5 summarizes the fitting parameters.

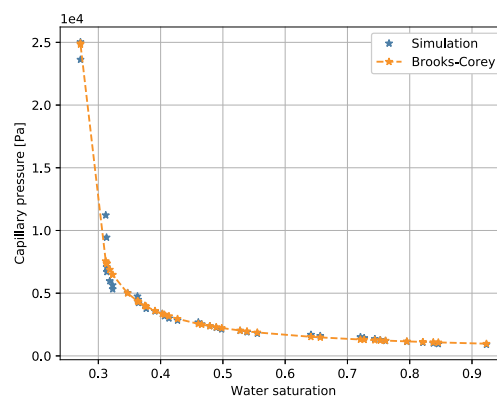
Fig. 11(a), at the LS stage start (solid line), the 72% water saturation points out that only the LS fluid can move through the network. In fact, the water relative permeability reaches 0.15, while the oil relative permeability is practically 0. Specifically, when $s_w = 72\%$, the oil saturation is 28%. This saturation value is known as critical oil saturation; that is, the saturation at which the oil begins to flow as the oil saturation increases. As water saturation decreases, the water relative permeability also decreases, while the oil relative permeability increases. Another particular point on the relative permeability curve is $s_w = 26\%$, because at this saturation the water relative permeability becomes zero and the oil relative permeability is the maximum. This saturation is the critical water saturation and can be greater than or equal to the irreducible water saturation. At the LSWF end, the dashed line curves in Fig. 11(a) show a slight shift to the right, compared to the initial curves (solid lines). Regarding the initial state, the system has a subtle change in wettability, the curve crossing point moves from $s_w = 0.66$ to 0.68 . Moreover, prior the oil becomes mobile and comparing the initial state to the final, the water relative permeability endpoint moves from 0.15 to 0.40. Finally, the k_r curves for HS and LS are fitted Fig. 11(b) and (c), respectively, and the fitting parameters are summarized in Table 5.



(a) Capillary pressure



(b) Fitted HS capillary pressure curve



(c) Fitted LS capillary pressure curve

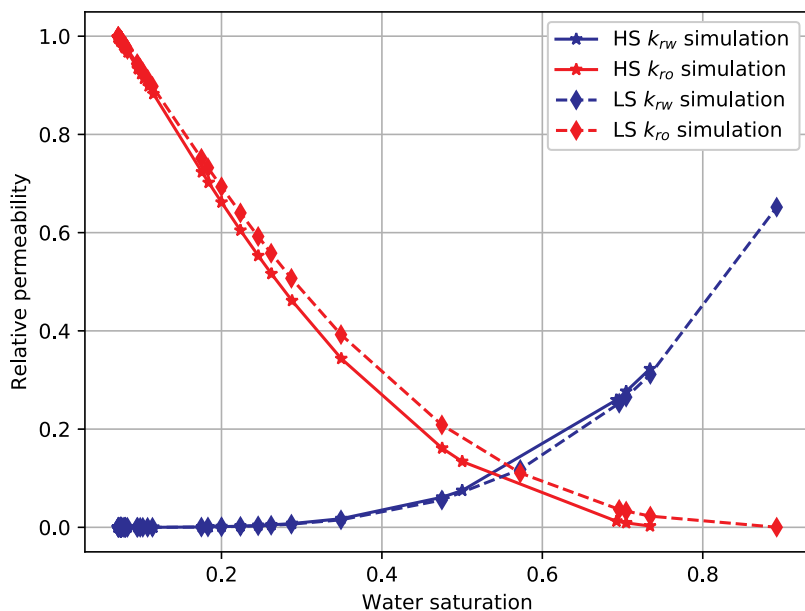
Fig. 10. Capillary pressure curves for Case 2. (a) Capillary pressure curves showing the LSWF effect. The red curve is for HS, while the blue curve is for LS. Fitted Brooks-Corey $p_c(s_w)$ models for (b) HS (c) LS. The blue points represent the values calculated in the primary drainage algorithm. The orange points are obtained using the fitted model. The dashed orange line shows the fitted curve trend. (For interpretation of the references to colour in this figure legend, the reader is referred to the Web version of this article.)

6. Conclusions

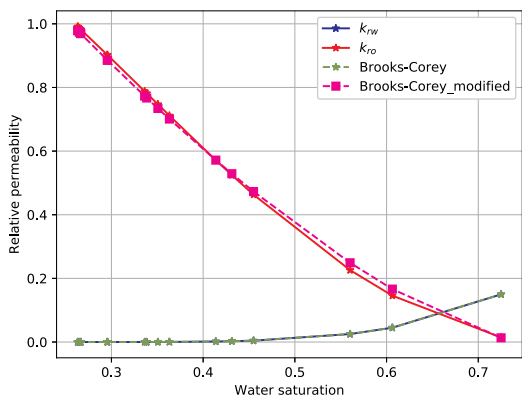
We have introduced a pore network based methodology to study the salinity effect on capillary pressure and relative permeability curves. Similarly, we formulated, implemented, and validated an advective-diffusive salinity transport model for pore networks. This model computes the salinity concentration values both in pores and throats. Since throats control the capillary pressure, knowing the throat salinity concentration allows us to evaluate the salinity impact on the capillary pressure curves. The way we associate the salinity and the capillary pressure is through the contact angle, which is a linear function of the

salinity concentration. The wettability of the network is modified by the changes in the contact angle, which in turn depends on the salinity. By reducing salinity the system becomes more water wet. By applying the methodology to two cases, one for a sandstone sample and the other for a carbonate sample, it has been demonstrated that our methodology can be used as a tool to rapidly estimate effective flow properties, which is an advantage over experimental procedures.

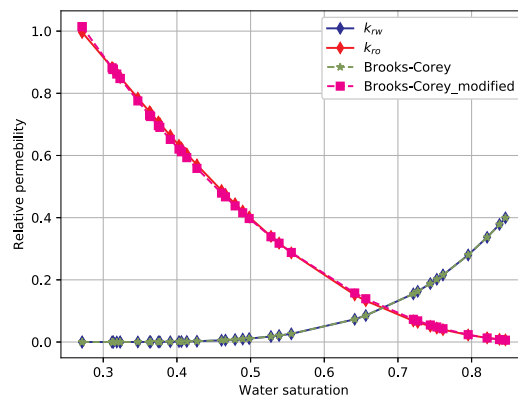
Finally, some requirements, limitations or possible improvements to our model should be mentioned. It should be considered that, (i) detailed information on the microscopic porous network structure is required; it can be obtained by micro CT scanning using some few



(a) Relative permeability



(b) Fitted HS relative permeability



(c) Fitted LS relative permeability

Fig. 11. Relative permeability curves for Case 2. (a) The red lines show the oil relative permeability k_{ro} and the blue lines the water relative permeability k_{rw} . Solid lines correspond to HS and dashed lines to LS, and original data are in red and blue. The curves were fitted at the end of the (b) HS and (c) LS stages. In curve fitting, a Brooks-Corey k_{rw} model (green line) and a modified Brooks-Corey k_{ro} model (pink line) were used. (For interpretation of the references to colour in this figure legend, the reader is referred to the Web version of this article.)

selected small rock samples, thus representability of large rock sample can be always questioned. (ii) Experimental information on the contact angle value at high and at low salinity is also needed. (iii) Salinity modifications can induce changes in the dynamic properties (for example on fluid viscosity (Boujelben et al., 2018), or on the absolute permeability due to fines release and pore throats clogging (Coronado and Díaz-Viera, 2017)) this would force a time-dependent pressure

analysis. (iv) The presence of oil-water biphasic flow will affect the microscopic fluid displacement. Nevertheless, the model we have presented here provides fundamental bases for the development of a methodology to estimate the relative permeability and capillary pressure dependence on salinity, which would be of great benefit when implementing oil recovery schemes by LSWF.

Nomenclature

Subscripts

0	Initial
<i>e</i>	Effective
<i>i, j</i>	Pore index
<i>ij</i>	Throat index
<i>iny</i>	Injection
<i>p</i>	Pore
<i>t</i>	Throat

Greek symbols

κ	Hydraulic conductance
μ	Viscosity
θ	Contact angle

Symbols

<i>A</i>	Cross-sectional area
<i>D</i>	Diffusion coefficient
<i>I</i>	Pore and throat indexes
<i>K</i>	Absolute permeability
<i>L</i>	Network length
<i>l</i>	Throat length
<i>p</i>	Pressure
<i>Q</i>	Total flow
<i>q</i>	Flow rate
<i>r</i>	Radii
<i>t</i>	Time
<i>V</i>	Volume

Superscripts

<i>HS</i>	High salinity
<i>LS</i>	Low salinity

Appendix A. Validation

In this appendix the validation of the numerical code for the salinity convective-dispersive transport using a 1D network system is described. The analytical solution employed to validate Equation (5) and Equation (6) is that presented by van Genuchten and Alves (1982) for a pulse type injection. The equation is:

$$R \frac{\partial c}{\partial t} = D \frac{\partial^2 c}{\partial x^2} - V \frac{\partial c}{\partial x} \quad (\text{A.1})$$

Equation (A.1) is subjected to the initial and boundary conditions:

$$\begin{aligned} c(x, 0) &= c_0 \\ c(0, t) &= \begin{cases} c_{inj} & 0 < t < t_{inj} \\ 0 & t > t_{inj} \end{cases} \\ \frac{\partial c(L, t)}{\partial x} &= 0 \end{aligned} \quad (\text{A.2})$$

where, t_{inj} and c_{inj} are the injection time and the salinity concentration during an injection period, respectively. The concentration at initial time is denoted as c_0 . The semi-analytical solution of Equation (A.1) is:

$$c(x, t) = \begin{cases} c_0 + (c_{inj} - c_0)A(x, t) & 0 < t < t_{inj} \\ c_0 + (c_{inj} - c_0)A(x, t) - c_{inj}A(x, t) & t > t_{inj} \end{cases} \quad (\text{A.3})$$

where

$$A(x, t) = 1 - \sum_{m=1}^{\infty} \frac{2\beta_m \sin\left(\frac{\beta_m x}{L}\right) \exp\left[\frac{vx}{2D} - \frac{v^2 t}{4DR} - \frac{\beta_m^2 D t}{L^2 R}\right]}{\left[\beta_m^2 + \left(\frac{vL}{2D}\right)^2 + \frac{vL}{2D}\right]} \quad (\text{A.4})$$

and where the eigenvalues β_m are the positive roots of the equation:

$$\beta_m \cot(\beta_m) + \frac{vL}{2D} = 0 \tag{A.5}$$

Table A.8 Parameters used in validation.

Property	Value	Unit
Initial concentration c_0	0	ppm
Injection concentration c_{inj}	200	ppm
Domain length L	1E-03	m
Injection time s	500, 50, and 5	s
Final time t_f	1000, 100, and 10	s
Time step Δt	1, 0.1, and 0.01	s
Injection velocity v	1.38E-04	m/s
Diffusion coefficient D	2.06E-08	m ² /s
R	1	

In our validation, a 10-pore one-dimensional network and ideal conditions are established. The considered parameters are summarized in Table A.8. Three 1000-iteration simulations were run for different time steps Δt , here 1, 0.1, and 0.01 [s] were employed. In this way, 1000, 100, and 10 [s] were considered as simulation times. To compare obtained results, concentration values at the outlet boundary were plotted for each time step (Fig. A.12).

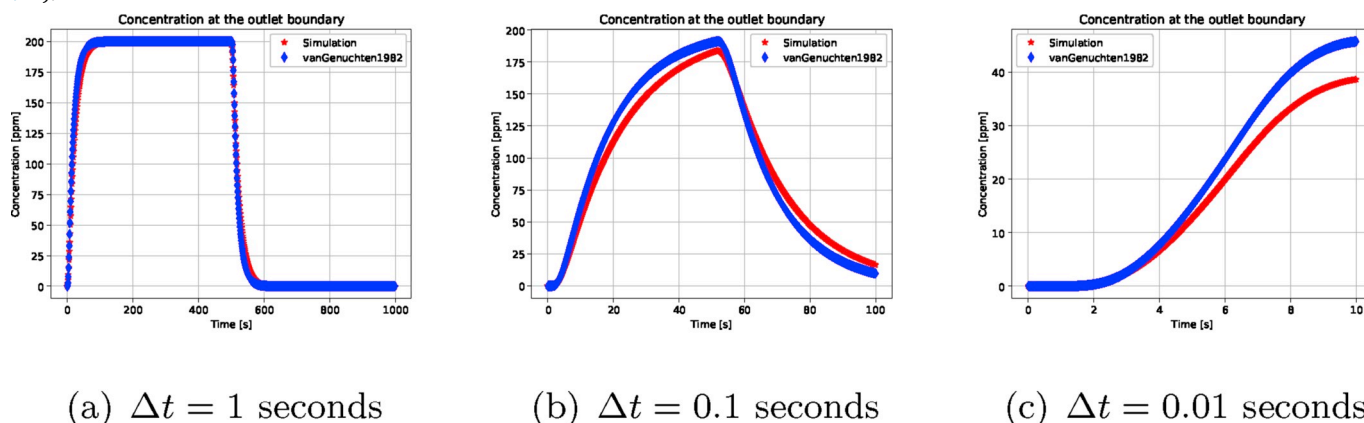


Fig. A.12. Concentration at the outlet boundary for different time steps. (a) $\Delta t = 1$ [s], (b) $\Delta t = 0.1$ [s], and (c) $\Delta t = 0.01$ [s]. The plots show a comparison between the numerical simulation (red line) and the semi-analytical solution (blue line).

The comparison between the numerical simulation and the semi-analytical solution is shown in Fig. A.12(a), (b) and (c), where the solution using $\Delta t = 1, 0.1,$ and 0.01 s, is respectively shown. By decreasing time step, Equation (5) and Equation (6) approach to the semi-analytical model. However, when $\Delta t = 0.01$ [s], the curves become separated at $t > 5$ [s]. But, since the mixtures are perfect and the reactions are neglected within pores and throats, this work does not require considering time steps below the thousandths of a second. Finally, according to computed errors summarized in Table A.9, it is agreed that the model (Equation (5) and Equation (6)) is validated, providing approximate values to the semi-analytical solution are obtained.

Table A.9 Computed error (%) from the numerical simulation and the semi-analytical solution.

Δt [s]	Absolute error	Relative error	Mean absolute error	Mean squared error
1	12	812	1	3
0.1	5	777	2	8
0.01	7	228	3	17

Appendix B. Modeling methodology using pore network models

In the literature, it has not been found a workflow that describes step by step the application of pore network models; however, common practices have been recognized. By following this review, fundamental procedures and techniques can be integrated and a methodology becomes apparent. It is noteworthy that each methodology stage can be divided into more fields, thus allowing a better study range (Martínez-Mendoza, 2016). In Fig. B.13, the solid red line points out the proposed methodology. However, depending on the ongoing stage, deviations from the proposed flow can be followed (dotted black lines). For example, a pore network can be generated directly from data acquisition (extracted networks) without performing statistical analysis. Likewise, it is possible to create a network if the workflow starts from statistical analysis. Finally, after validation and uncertainty assessment, the workflow can turn back either data acquisition or statistical analysis in order to perform new realizations. The methodology stages are described below.

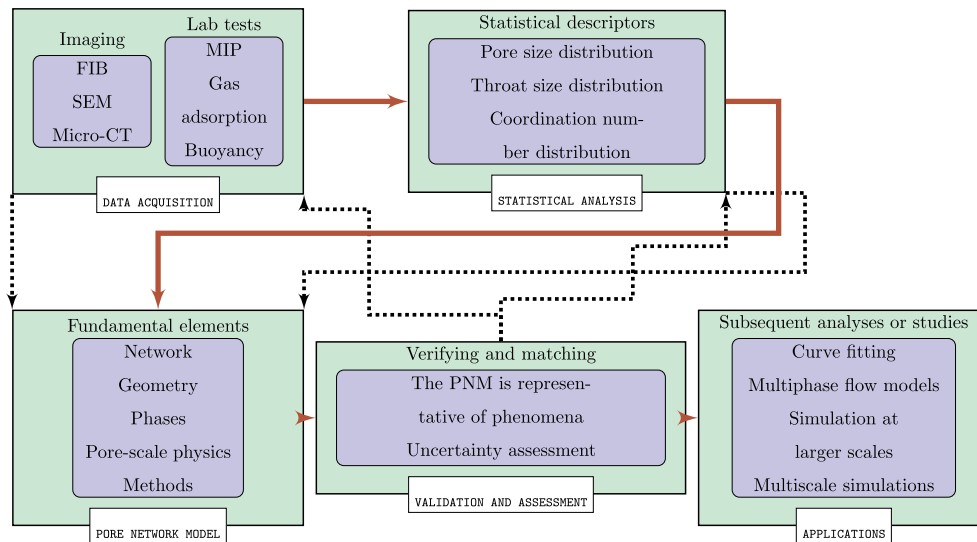


Fig. B.13. Modeling methodology using pore networks. The methodology comprises five fundamental stages: data acquisition, statistical analysis of pore structure properties, pore network model, validation and uncertainty assessment, and applications.

Data acquisition

In this stage, various properties that describe the porous medium, the fluids and the rock-fluid interactions are obtained. In pore network modeling, it becomes crucial to know the pore and the throat shapes and sizes, as well as the way in which these elements are connected. Therefore, the following pore and throat properties must be defined: spatial location, coordination number, area, inscribed diameter, perimeter, total length, volume, cross section, and shape factor. To characterize the porous medium there are high resolution imaging techniques such as scanning electron microscopy (1 – 20 [nm]), focused ion beam (<1 [nm]), confocal laser scanning microscopy (~1 [μm]), X-ray computed micro-tomography (1 – 200 [μm]), and nuclear magnetic resonance (2 [nm] – 1 [μm]) (Dong, 2007; Xiong et al., 2016). Applying these image techniques, the pore and the throat sizes, the network node coordinates and their connections with other nodes are inferred. Finally, to characterize the fluids and the rock-fluid system, laboratory tests to measure density, viscosity, interfacial tension, and contact angle, among other properties, are performed.

Statistical analysis of pore structure properties

This stage involves performing statistical analysis to main medium structure properties (e.g., throat and pore sizes, and coordination number) to fit probability distribution functions. The probability distribution functions generate the aforementioned property values, and consequently, a porous media analogous to the original one can be achieved. In addition, performing network spatial statistical analysis to infer connectivity and percolation properties is highly recommended. With all this information it is possible different spatial realizations of the original sample.

Pore network model

From the previous stage an optimal framework for setting the fundamental pore network elements can be established. The complexity and detail with which the network and geometry are represented establish a starting point to formulate the pore-scale physics and consequently, the method scope. In principle, the pore network models can be generated from three-dimensional reconstructions of rock samples and from their respective extracted network and geometry. Although this technique for pore network generation is established, it results in reality that the required information and tools are not fully available. Further, working with a unique extracted network could yield a narrow study window, and the model cannot be representative. Hence, the statistical analysis represents an attractive option to generate different realizations for the network and the geometry. Finally, the simulations using these models can help to build a reliability window, which provides a value range that a desired property can take for a particular medium (e.g., absolute permeability, capillary pressure, relative permeability).

Validation and uncertainty assessment

The validations of properties such as porosity, absolute permeability, capillary pressure, and relative permeability, can be achieved by comparing them against the corresponding laboratory test data. This comparison allows us to verify that the implemented pore network model is representative of the phenomena. In addition, an uncertainty evaluation can be obtained by multiple simulations exploring the pore network parameters (e.g., the throat and pore size distributions).

Application in multiphase flow models

Finally, the obtained porosity, absolute permeability, capillary pressure, and relative permeability values can be used in subsequent analyzes, such as curve fitting, multiphase flow models, simulations at larger scales, and multiscale simulations.

Appendix C. Supplementary data

Supplementary data to this article can be found online at <https://doi.org/10.1016/j.petrol.2019.106253>.

References

- Acharya, R., Van der Zee, S., Leijnse, A., 2005. Transport modeling of nonlinearly adsorbing solutes in physically heterogeneous pore networks. *Water Resour. Res.* 41 (2), 11. <https://doi.org/10.1029/2004WR003500>.
- Aker, E., Maloy, K., Hansen, A., Batrouni, G., 1998. A two-dimensional network simulator for two-phase flow in porous media. *Transp. Porous Media* 32 (2), 163–186. <https://doi.org/10.1023/A:1006510106194>.
- Al-Shalabi, E.W., Sepehrmoori, K., 2016. A comprehensive review of low salinity/engineered water injections and their applications in sandstone and carbonate rocks. *J. Pet. Sci. Eng.* 139 (1), 137–161. <https://doi.org/10.1016/j.petrol.2015.11.027>.
- Aladasani, A., Bai, B., Wu, Y.-S., Salehi, S., 2014. Studying low-salinity waterflooding recovery effects in sandstone reservoirs. *J. Pet. Sci. Eng.* 120 (1), 39–51. <https://doi.org/10.1016/j.petrol.2014.03.008>.
- Arns, J., Robins, V., Sheppard, A., Sok, R., Pinczewski, W., Knackstedt, M., 2004. Effect of network topology on relative permeability. *Transp. Porous Media* 55 (11), 21–46. <https://doi.org/10.1023/B:TIPM.0000007252.68488.43>.
- Austad, T., 2013. Water-based EOR in carbonates and sandstones: new chemical understanding of the EOR potential using “smart water”. In: Sheng, J.J. (Ed.), *Enhanced Oil Recovery Field Case Studies* Chapter 13. Gulf Professional Publishing, pp. 301–335. <https://doi.org/10.1016/B978-0-12-386545-8.00013-0>.
- Berkowitz, B., Ewing, R., 1998. Percolation theory and network modeling applications in soil physics. *Surv. Geophys.* 19 (1), 23–72. <https://doi.org/10.1023/A:1006590500229>.
- Blunt, M., Bijeljic, B., Dong, H., Gharbi, O., Iglauer, S., Mostaghimi, P., 2013. Pore-scale imaging and modeling. *Adv. Water Resour.* 51 (1), 197–216. <https://doi.org/10.1016/j.advwatres.2012.03.003>.
- Blunt, M., Jackson, M., Piri, M., Valvatne, P., 2002. Detailed physics, predictive capabilities and macroscopic consequences for pore-network models of multiphase flow. *Adv. Water Resour.* 25 (8–12), 1069–1089. [https://doi.org/10.1016/S0309-1708\(02\)00049-0](https://doi.org/10.1016/S0309-1708(02)00049-0).
- Bolandtaba, S.F., Skauge, A., 2011. Network modeling of eor processes: a combined invasion percolation and dynamic model for mobilization of trapped oil. *Transp. Porous Media* 89 (3), 357–382. <https://doi.org/10.1007/s11242-011-9775-0>.
- Boujelben, A., McDougall, S., Watson, M., Bondino, I., Agenet, N., 2018. Pore network modelling of low salinity water injection under unsteady-state flow conditions. *J. Pet. Sci. Eng.* 165 (1), 462–476. <https://doi.org/10.1016/j.petrol.2018.02.040>.
- Broadbent, S., Hammersley, J., 1957. Percolation processes I. Crystals and mazes. *Math. Proc. Camb. Philos. Soc.* 53 (3), 629–641. <https://doi.org/10.1017/S0305004100032680>.
- Burdine, N., 1953. Relative permeability calculations from pore size distribution data. *SPE* 5 (3), 71–78. <https://doi.org/10.2118/225-G>.
- Coronado, M., Díaz-Viera, M., 2017. Modeling fines migration and permeability loss caused by low salinity in porous media. *J. Pet. Sci. Eng.* 150, 355–365. <https://doi.org/10.1016/j.petrol.2016.12.021>.
- Dai, S., Santamarina, J., 2013. Water retention curve for hydrate-bearing sediments. *Geophys. Res. Lett.* 40 (21), 5637–5641. <https://doi.org/10.1002/2013GL057884>.
- Dang, C., Nghiem, L., Chen, Z., Nguyen, Q., 2013. Modeling low salinity waterflooding: ion exchange, geochemistry and wettability alteration. *SPE*, 166447-MS 1–22. <https://doi.org/10.2118/166447-MS>.
- Dias, M., Wilkinson, D., 1986. Percolation with trapping. *J. Phys. A Math. Gen.* 19 (15), 3131–3146. <https://doi.org/10.1088/0305-4470/19/15/034>.
- Dong, H., 2007. *Micro-ct Imaging and Pore Network Extraction*. Imperial College London, pp. 1–213 Unpublished thesis.
- Dong, H., Touati, M., Blunt, M., 2007. Pore network modeling: analysis of pore size distribution of arabian core samples. *SPE*, 105156-MS 1–5. <https://doi.org/10.2118/105156-MS>.
- Emetadi, A., Khodapanah, E., Tabatabaei-Nejad, S.A., 2017. Modelling low-salinity waterflooding: effect of divalent cations and capillary pressure. *J. Pet. Sci. Eng.* 149 (1), 1–8. <https://doi.org/10.1016/j.petrol.2016.10.012>.
- Ewing, R.E., Wang, H., 2001. A summary of numerical methods for time-dependent advection-dominated partial differential equations. *J. Comput. Appl. Math.* 128 (1), 423–445. [https://doi.org/10.1016/S0377-0427\(00\)00522-7](https://doi.org/10.1016/S0377-0427(00)00522-7).
- Fazeli, M., Hinebaugh, J., Bazylak, A., 2016. Incorporating embedded microporous layers into topologically equivalent pore network models for oxygen diffusivity calculations in polymer electrolyte membrane fuel cell gas diffusion layers. *Electrochim. Acta* 216 (1), 364–375. <https://doi.org/10.1016/j.electacta.2016.08.126>.
- van Genuchten, M., Alves, W., 1982. Analytical solutions of the one-dimensional convective-dispersive solute transport equation. United states department of agriculture, economic research service. *Technical Bulletin* 1661, 1–152.
- Gharbi, O., Blunt, M.J., 2012. The impact of wettability and connectivity on relative permeability in carbonates: a pore network modeling analysis. *Water Resour. Res.* 48 (12), 1–14. <https://doi.org/10.1029/2012WR011877>.
- Gostick, J., Aghighi, M., Hinebaugh, J., Tranter, T., Hoeh, M.A., Day, H., Spellacy, B., Sharqawy, M.H., Bazylak, A., Burns, A., Lehnert, W., Putz, A., 2016. Openpnm: a pore network modeling package. *Comput. Sci. Eng.* 18 (4), 60–74. <https://doi.org/10.1109/MCSE.2016.49>.
- Gostick, J., Ioannidis, M., Fowler, M., Pritzker, M., 2007. Pore network modeling of fibrous gas diffusion layers for polymer electrolyte membrane fuel cells. *J. Power Sources* 173 (1), 277–290. <https://doi.org/10.1016/j.jpowsour.2007.04.059>.
- Gostick, J.T., Fowler, M.W., Ioannidis, M.A., Pritzker, M.D., Volkovich, Y., Sakars, A., 2006. Capillary pressure and hydrophilic porosity in gas diffusion layers for polymer electrolyte fuel cells. *J. Power Sources* 156 (2), 375–387. <https://doi.org/10.1016/j.jpowsour.2005.05.086>.
- Gostick, J.T., Weber, A.Z., 2015. Resistor-network modeling of ionic conduction in polymer electrolytes. *Electrochim. Acta* 179 (1), 137–145. <https://doi.org/10.1016/j.electacta.2015.03.126>.
- Hammond, P., Unsal, E., 2012. A dynamic pore network model for oil displacement by wettability-altering surfactant solution. *Transp. Porous Media* 92 (3), 789–817. <https://doi.org/10.1007/s11242-011-9933-4>.
- Hunt, A., Ewing, R., 2009. *Percolation Theory for Flow in Porous Media*. Lecture Notes in Physics. Springer <https://doi.org/10.1007/978-3-540-89790-3>.
- ICL, 2014. Imperial College Consortium on Pore-Scale Modelling: C2 Carbonate. PERM <https://doi.org/10.6084/m9.figshare.1189258.v1>. <http://www.imperial.ac.uk/earth-science/research/research-groups/perm/research/pore-scale-modelling/micro-ct-images-and-networks/carbonate-c2/>.
- ICL, 2014. Imperial College Consortium on Pore-Scale Modelling: S1 Sandstone. PERM <https://doi.org/10.6084/m9.figshare.1189274.v1>. <http://www.imperial.ac.uk/earth-science/research/research-groups/perm/research/pore-scale-modelling/micro-ct-images-and-networks/carbonate-c2/>.
- Ioannidis, M., Chatzis, I., 1993. Network modelling of pore structure and transport properties of porous media. *Chem. Eng. Sci.* 48 (3), 951–972. [https://doi.org/10.1016/0009-2509\(93\)80333-L](https://doi.org/10.1016/0009-2509(93)80333-L).
- Jang, J., Santamarina, J., 2014. Evolution of gas saturation and relative permeability during gas production from hydrate-bearing sediments: gas invasion vs. gas nucleation. *J. Geophys. Res. Solid Earth* 119 (1), 116–126. <https://doi.org/10.1002/2013JB010480>.
- Jerauld, G., Webb, K., Lin, C., Seccombe, J., 2008. Modeling low-salinity waterflooding. *SPE* 11 (6), 1000–1012. <https://doi.org/10.2118/102239-PA>.
- Kang, D., Yun, T., Kim, K., Jang, J., 2016. Effect of hydrate nucleation mechanisms and capillarity on permeability reduction in granular media. *Geophys. Res. Lett.* 43 (17), 9018–9025. <https://doi.org/10.1002/2016GL070511>.
- Kim, S., Santamarina, J., 2015. Reactive fluid flow in CO₂ storage reservoirs: a 2-d pore network model study. *Greenhouse Gas Sci. Technol.* 5 (1), 462–473. <https://doi.org/10.1002/ghg.1487>.
- Li, K., Horne, R.N., 2006. Comparison of methods to calculate relative permeability from capillary pressure in consolidated water-wet porous media. *Water Resour. Res.* 42 (6), 1–9. <https://doi.org/10.1029/2005WR004482>.
- Lu, C., Yortsos, Y., 2001. A pore-network model of in-situ combustion in porous media. *SPE*, 69705-MS 1–16. <https://doi.org/10.2118/69705-MS>.
- Mahabadi, N., Dai, S., Seol, Y., Sup Yun, T., Jang, J., 2016. The water retention curve and relative permeability for gas production from hydrate-bearing sediments: pore-network model simulation. *Geochem. Geophys. Geosyst.* 17 (8), 3099–3110. <https://doi.org/10.1002/2016GC006372>.
- Mahabadi, N., Jang, J., 2014. Relative water and gas permeability for gas production from hydrate-bearing sediments. *Geochem. Geophys. Geosyst.* 15 (6), 2346–2353. <https://doi.org/10.1002/2014GC005331>.
- Mahabadi, N., Zheng, X., Jang, J., 2016. The effect of hydrate saturation on water retention curves in hydrate-bearing sediments. *Geophys. Res. Lett.* 43 (9), 4279–4287. <https://doi.org/10.1002/2016GL068656>.
- Mahani, H., Keya, A.L., Berg, S., Nasralla, R., 2017. Electrokinetics of carbonate/brine interface in low-salinity waterflooding: effect of brine salinity, composition, rock type, and pH on ζ -potential and a surface-complexation model. *SPE* 22 (1), 1–16. <https://doi.org/10.2118/181745-PA>.
- Mahani, H., Sorop, T., Ligthelm, D., Brooks, D., Vledder, P., Mozahem, F., Ali, Y., 2011. Analysis of field responses to low-salinity waterflooding in secondary and tertiary mode in Syria. *SPE*, 142960-MS 1–14. <https://doi.org/10.2118/142960-MS>.
- Martínez-Mendoza, E.G., 2016. *Pore Network Models for Obtaining Effective Flow and Transport Properties in Petroleum Reservoirs*. Universidad Nacional Autónoma de México, Faculty of Engineering (Bachelor), pp. 103 Unpublished thesis.
- Martínez-Mendoza, E.G., 2018. *Rock-fluid Property Estimation through Pore Network Models for Low Salinity Waterflooding Process Simulation*. Universidad Nacional Autónoma de México, Graduate Program in Earth Sciences (Master of Science), pp. 146 Unpublished thesis.
- Martínez-Mendoza, E.G., Díaz-Viera, M.A., 2018. Study of the Impact of Salinity Change in a Lswf Process on Capillary Pressure and Relative Permeability Curves by Flow and Transport Modeling at Pore Network Scale. National Institute of Copyright, Mexico, pp. 1–45 Record number: 03-2018-121914143500-01.
- Mostaghimi, P., Bijeljic, B., Blunt, M., 2012. Simulation of flow and dispersion on pore-space images. *SPE* 17 (4), 11. <https://doi.org/10.2118/135261-PA>.
- Moustafa, E., Noah, A., Beshay, K., Sultan, L., Essam, M., Nouh, O., 2015. Investigating the effect of various nanomaterials on the wettability of sandstone reservoir. *World J. Eng. Technol.* 3 (1), 116–126. <https://doi.org/10.4236/wjet.2015.33013>.
- Nasralla, R.A., Mahani, H., van der Linde, H.A., Marcellis, F.H., Masalmeh, S.K., Sergienko, E., Brussee, N.J., Pieterse, S.G., Basu, S., 2018. Low salinity waterflooding for a carbonate reservoir: experimental evaluation and numerical interpretation. *J. Pet. Sci. Eng.* 164 (1), 640–654. <https://doi.org/10.1016/j.petrol.2018.01.028>.

- Okabe, H., Blunt, M.J., 2004. Prediction of permeability for porous media reconstructed using multiple-point statistics. *Phys. Rev. E* 70 (6), 066135. <https://doi.org/10.1103/PhysRevE.70.066135>.
- Omekeh, A., Friis, H., Fjelde, S., Evje, I., 2012. Modeling of ion-exchange and solubility in low salinity water flooding. *SPE*, 154144-MS 1–13. <https://doi.org/10.2118/154144-MS>.
- Qin, C.Z., Hassanizadeh, S.M., 2015. Pore-network Modeling of Solute Transport and Biofilm Growth in Porous Media. *Transp. Porous Media* 110, 345–367. <https://doi.org/10.1007/s11242-015-0546-1>.
- Raeni, A.Q., Bijeljic, B., Blunt, M.J., 2017. Generalized network modeling: network extraction as a coarse-scale discretization of the void space of porous media. *Phys. Rev. E* 96 (1), 17. <https://doi.org/10.1103/PhysRevE.96.013312>.
- Raeni, A.Q., Bijeljic, B., Blunt, M.J., 2018. Generalized network modeling of capillary-dominated two-phase flow. *Phys. Rev. E* 97 (2), 20. <https://doi.org/10.1103/PhysRevE.97.023308>.
- Raoof, A., 2011. *Reactive/Adsorptive Transport in (Partially-) Saturated Porous Media; from Pore Scale to Core Scale*. Geologica Ultraeicina, first ed. Utrecht University, Geosciences Faculty, Earth sciences department.
- Raoof, A., Nick, H., Hassanizadeh, S., Spiers, C., 2013. Poreflow: a complex pore-network model for simulation of reactive transport in variably saturated porous media. *Comput. Geosci.* 61 (1), 160–174. <https://doi.org/10.1016/j.cageo.2013.08.005>.
- Raoof, A., Nick, H.M., Hassanizadeh, S.M., Spiers, C.J., 2014. Pore-network modeling of multi-component reactive transport under (variably-) saturated conditions. In: Al-Khoury, R., Bundschuh, J. (Eds.), *Computational Models for CO2 Geo-Sequestration & Compressed Air Energy Storage* Sustainable Energy Developments Chapter 4, first ed. CRC Press, London, pp. 137–170.
- Rodríguez, F., Teysier, J., 1974. Permeabilidades relativas en función de la presión capilar y las saturaciones efectivas. *Ing. Pet.* 14 (3), 110–127.
- Sadeghi, M., Aghighi, M., Barralet, J., Gostick, J., 2017. Pore network modeling of reaction-diffusion in hierarchical porous particles: the effects of microstructure. *Chem. Eng. J.* 330 (1), 1002–1011. <https://doi.org/10.1016/j.cej.2017.07.139>.
- Sahimi, M., 2011. *Flow and Transport in Porous Media and Fractured Rock*, second ed. Wiley-VCH.
- Sanaei, A., Tavassoli, S., Sepehrnoori, K., 2018. Investigation of modified water chemistry for improved oil recovery: application of dlvo theory and surface complexation model. *SPE* 190017-MS, 1–27. <https://doi.org/10.2118/190017-MS>.
- Sheng, J., 2014. Critical review of low-salinity waterflooding. *J. Pet. Sci. Eng.* 120 (1), 216–224. <https://doi.org/10.1016/j.petrol.2014.05.026>.
- Sohal, M.A., Thyne, G., Sogaard, E.G., 2016. Review of recovery mechanisms of ionically modified waterflood in carbonate reservoirs. *Energy Fuels* 30 (3), 1904–1914. <https://doi.org/10.1021/acs.energyfuels.5b02749>.
- Sorbie, K., Collins, I., 2010. A proposed pore-scale mechanism for how low salinity waterflooding works. *SPE*, 129833-MS 1–18. <https://doi.org/10.2118/129833-MS>.
- Tang, G., Morrow, N., 1997. Salinity, temperature, oil composition, and oil recovery by waterflooding. *SPE* 12 (2), 1–8. <https://doi.org/10.2118/36680-PA>.
- Tranter, T., Gostick, J., Burns, A., Gale, W., 2016. Pore network modeling of compressed fuel cell components with openpnm. *Fuel Cells* 16 (4), 504–515. <https://doi.org/10.1002/fuce.201500168>.
- Tranter, T., Gostick, J., Burns, A., Gale, W., 2018. Capillary hysteresis in neutrally wettable fibrous media: a pore network study of a fuel cell electrode. *Transp. Porous Media* 121 (3), 597–620. <https://doi.org/10.1007/s11242-017-0973-2>.
- Valvatne, P., Piri, M., Lopez, X., Blunt, M., 2005. Predictive pore-scale modeling of single and multiphase flow. *Transp. Porous Media* 58 (1–2), 23–41. <https://doi.org/10.1007/s11242-004-5468-2>.
- Watson, M., Bondino, I., Hamon, G., McDougall, S., 2011. A pore-scale investigation of low-salinity waterflooding in porous media: uniformly wetted systems. *Transp. Porous Media* 118 (2), 201–223. <https://doi.org/10.1007/s11242-017-0854-8>.
- Webb, K., Black, C., Edmonds, I., 2005. *Low Salinity Oilrecovery: the Role of Reservoir Condition Corefloods*. EAGE Symposium on Improved Oil Recovery. Paper C18.
- Webb, K.J., Black, C.J.J., Al-Ajeel, H., 2004. Low salinity oil recovery - log-inject-log. *SPE*, 89379-MS 1–7. <https://doi.org/10.2118/89379-MS>.
- Wu, Y., Bai, B., 2009. Efficient simulation for low salinity waterflooding in porous and fractured reservoirs. *SPE*, 118830-MS 1–13. <https://doi.org/10.2118/118830-MS>.
- Xie, C., Raeni, A.Q., Wang, Y., Blunt, M.J., Wang, M., 2017. An improved pore-network model including viscous coupling effects using direct simulation by the lattice Boltzmann method. *Adv. Water Resour.* 100, 26–34. <https://doi.org/10.1016/j.advwatres.2016.11.017>.
- Xiong, Q., Baychev, T.G., Jivkov, A.P., 2016. Review of pore network modelling of porous media: experimental characterisations, network constructions and applications to reactive transport. *J. Contam. Hydrol.* 192 (1), 101–117. <https://doi.org/10.1016/j.jconhyd.2016.07.002>.
- Xu, Q., Long, W., Jiang, H., Zan, C., Huang, J., Chen, X., Shi, L., 2018. Pore-scale modelling of the coupled thermal and reactive flow at the combustion front during crude oil in-situ combustion. *Chem. Eng. J.* 350 (1), 776–790. <https://doi.org/10.1016/j.cej.2018.04.114>.
- Yildiz, H.O., Morrow, N.R., 1996. Effect of brine composition on recovery of moutray crude oil by waterflooding. *J. Pet. Sci. Eng.* 14 (3–4), 159–168. [https://doi.org/10.1016/0920-4105\(95\)00041-0](https://doi.org/10.1016/0920-4105(95)00041-0).
- Yiotis, A., Stubos, A., Boudouvis, A., Yortsos, Y., 2001. A 2-d pore-network model of the drying of single-component liquids in porous media. *Adv. Water Resour.* 24 (3–4), 439–460. [https://doi.org/10.1016/S0309-1708\(00\)00066-X](https://doi.org/10.1016/S0309-1708(00)00066-X).
- Yousef, A.A., Al-Saleh, S.H., Al-Kaabi, A., Al-Jawfi, M.S., 2011. Laboratory investigation of the impact of injection-water salinity and ionic content on oil recovery from carbonate reservoirs. *SPE* 14 (5), 1–16. <https://doi.org/10.2118/137634-PA>.
- Yousef, A.A., Liu, J.S., Blanchard, G.W., Al-Saleh, S., Al-Zahrani, T., Al-Zahrani, R.M., Al-Tammar, H.I., Al-Mulhim, N., 2012. *Smart Waterflooding: Industry*. *SPE*, 159526-MS, pp. 1–26. <https://doi.org/10.2118/159526-MS>.
- Zhao, W., Ioannidis, M.A., 2011. Gas exsolution and flow during supersaturated water injection in porous media: I. pore network modeling. *Adv. Water Resour.* 34 (1), 2–14. <https://doi.org/10.1016/j.advwatres.2010.09.010>.